

Study of Dynamics of Water Droplet Freezing

by

Lalitha Ganesh Prabhu Komaragiri

A thesis submitted in partial fulfillment of the requirements for the degree of

Master of Science

Department of Mechanical Engineering
University of Alberta

© Lalitha Ganesh Prabhu Komaragiri, 2024

Abstract

This thesis delves into the intricate dynamics of water droplet freezing, a phenomenon with profound implications across a spectrum of fields including climate science, anti-icing technologies, and cryogenic 3D printing. The influence of heat transfer on the wettability and freezing processes of water droplets was investigated. Utilizing a jet-based dosing system, droplets were deposited onto precooled substrates of varying thermal conductivities. The simultaneous spreading and freezing dynamics of a water droplet was investigated. The spreading and freezing stages of droplets created by a continuous jet have been outlined. Thermal imaging showed that the effect of supercooling was absent in the dosing with jet-based methods. A theoretical model was proposed to elucidate the temporal evolution of the three-phase contact line (TPCL). The model was nondimensionalized using appropriate length, time, and temperature scales. The findings demonstrate a pivotal relationship between the Stefan number and the spreading rate. The time delay at the beginning of freezing is significantly influenced by the Ste number. The universal behavior of the tip-cone angle created by the frozen water droplet was also analyzed. It was observed that, for a particular density ratio, the ratio between the height of the solidified droplet and the liquid droplet remains constant, irrespective of the droplet's shape. This can be considered as the true universality of the frozen droplet. This was observed for the case of symmetric and asymmetric droplets. A series of parabolic flights were performed that simulate microgravity, martian gravity, and hypergravity to investigate the influence of body forces on the universal behavior of the frozen water droplets. In the present study, a more general theoretical model that can predict the solid-liquid height ratio, called

the “two triangle” approach, was proposed. Finally, the current study aims to investigate the freezing dynamics and morphology by examining the process of successive droplet dosing onto a cold substrate and the formation of column-like ice structures at a macroscopic level. Using a jet-based dosing mechanism, we meticulously controlled the deposition of water droplets onto a smooth copper substrate maintained at subzero temperatures. The experimental design systematically varied the volume and frequency of the droplets. Different final column structures were observed under different experimental conditions. Real-time shadowgraphy and thermal imaging were utilized to capture morphological and thermal changes during the freezing process. The effects of remelting and heat accumulation on the bonding and the form of the column-ice structure were investigated. Lastly, an optimized volume and frequency sequence was suggested to obtain ideal bonding conditions.

Preface

All work summarized in this thesis is an original work by Lalitha Ganesh Prabhu Komaragiri under the supervision of Dr. Prashant R Waghmare. Lalitha Ganesh Prabhu Komaragiri was responsible for concept formulation, experimental design, conducting the experiments, data analysis, data interpretation, developing the theoretical framework and analysis, and writing the manuscripts. Dr. Prashant R. Waghmare supervised all the work presented by Lalitha Ganesh Prabhu Komaragiri and was involved with conceptualization and editing of the manuscripts.

A version of Chapter 2 of this thesis has been prepared for submission to peer-reviewed journal: International Journal of Heat and Mass Transfer, as “Ganesh P Komaragiri, Abrar Ahmed, Prashant R. Waghmare, Freezing of a spreading droplet”. For the study of Chapter 2, Abrar Ahmed was involved with the necessary revisions of the manuscript and was involved in providing assistance in the experimental setup and developing the theoretical framework. A portion of Chapter 2 was presented at the “76th American Physical Society (APS) Division of Fluid Dynamics conference” by “Ganesh P Komaragiri, Abrar Ahmed, and Prashant R. Waghmare, A theoretical and experimental investigation of the simultaneous spreading and freezing of droplets” held in Washington, DC, USA from November 19th – 21st 2023.

A version of Chapter 3 of this thesis, along with some additional work from the coauthors, has been prepared for submission to another peer-reviewed journal (Physical Review Letter) for publication as “Ganesh P Komaragiri, Abrar Ahmed,

Farhad Ismail, Prashant R Waghmare, “Universality of frozen water drop”. Abrar Ahmed was responsible for concept formulation, theoretical analysis, experiments, data analysis, results evaluation, and was involved with the necessary revisions of the manuscript. Farhad Ismail was responsible for initial experimentation and preliminary theoretical modeling. Chapter 4 of this thesis is being prepared for peer-reviewed journal (Materials Letters) for publication as “Ganesh P Komaragiri, Abrar Ahmed, Dr. Prashant R Waghmare, Dynamics of Successive Water Droplet Freezing on Cold Substrates”. Abrar Ahmed was involved with the general discussion, providing assistance in the experimental setup and necessary revisions of the manuscript.

Acknowledgements

I want to begin by expressing my heartfelt gratitude to all wise individuals who have played a pivotal role in my journey towards completing my master's thesis. Without their unwavering support, I would not have reached this significant milestone. I am particularly grateful to Dr. Prashant R. Waghmare, my dedicated supervisor, for his exceptional guidance and support throughout my entire project. From the conceptualization of the entire project with the development of the experimental setup to the writing of the manuscripts, Dr. Waghmare's wealth of scientific knowledge, professionalism, and punctuality has been invaluable. The wisdom, patience, and benevolence he demonstrated during my master's program provided me with all the necessary tools to successfully complete my thesis. I believe myself to be fortunate to have had the opportunity to work under Dr. Waghmare's mentorship, and I express my sincere appreciation for his contributions to my academic journey.

I extend my gratitude to Abrar Ahmed for his exceptional support and encouragement, particularly throughout the experimental phase. His deep insights and spirit of collaboration have been instrumental in guiding me through my research endeavors. My sincere thanks also go to Ryan Bailey for his crucial support during this critical phase. I appreciate the camaraderie and assistance of my labmates, Vivek Kumar and Dr. Butunath. Their collaborative spirit and shared expertise have greatly enriched my research experience.

I am also grateful to my friends Prem Sai Akula, Sudhakar Chepuri, and Bhanu

Prasad Reddy P for their unwavering moral support. Their friendship and encouragement have been a source of strength and resilience throughout this journey.

Finally, my heartfelt appreciation goes to my parents, K Maheswar Prabhu and Dr. V.R. Jyotsna Kumari. Their unending love, encouragement, and support have been the foundation of all my achievements. They have been my guide light and the source of my strength, and I am forever indebted to them for their sacrifices and belief in me.

This journey would not have been as fulfilling without these remarkable individuals who have contributed significantly to both my personal and academic growth. I am forever grateful for their presence in my life.

Table of Contents

1	Introduction	1
1.1	Applications	2
1.2	Aim of the present work	4
1.3	Literature Review	5
1.3.1	Droplet spreading and freezing	5
1.3.2	Freezing dynamics of a water droplet	7
1.3.3	Successive droplet freezing	9
1.4	Thesis Outline	10
2	Freezing of a Spreading Droplet	12
2.1	Abstract	12
2.2	Introduction	13
2.3	Experimental description	16
2.3.1	Materials and methods	16
2.3.2	Uncertainty analysis	18
2.4	Results and Discussion	19
2.4.1	Jet-based drop deposition	19
2.4.2	Temperature profiles	22
2.4.3	Theoretical Model	25
2.4.4	Droplet spreading	30
2.4.5	Freezing dynamics	34
2.5	Conclusion	38

3	Universality of Frozen Water Droplet	39
3.1	Abstract	39
3.2	Introduction	40
3.3	Experimental description	42
3.4	Theroretical Model	43
3.4.1	Tip angle vs density ratio	43
3.4.2	Two Triangle Approach	44
3.4.3	Heat Transfer Model	47
3.4.4	Average contact angle approach	48
3.5	Results and discussion	51
3.6	Conclusion	56
4	Dynamics of Successive Water Droplet Freezing	57
4.1	Abstract	57
4.2	Introduction	58
4.3	Experimental setup	60
4.4	Results and Discussion	62
4.4.1	Ice column Morphology	65
4.4.2	Remelting and bonding	66
4.4.3	Effect of heat accumulation	69
4.5	Conclusion	72
5	Conclusion and Future Work	73
5.1	Conclusion	73
5.2	Future work	75
5.2.1	Ice-printing	75
	Bibliography	77
	Appendix A:	84

List of Tables

2.1	Physical properties of the substrates and the liquid used for current study	18
2.2	The dynamic contact angle during the propagation of TPCL until it reaches equilibrium	33
4.1	Volume and frequency used for the current study are compiled for four cases. The study was presented in four different experimental settings, each varying the volume (V) and frequency (f) of the droplets in a controlled manner. The subscripts ‘ c ’ and ‘ v ’ denote constant and variable, respectively.	64

List of Figures

1.1	(a) Schematic representation of the temperature transition during the freezing of a droplet.	8
2.1	Schematic diagram of the experimental setup.	16
2.2	(a) Schematic representation of the stages involved in jet-based dosing system. Also represents the nomenclature used for current study. (b) and (c) shows the shadow graphic and thermal experimental images for the respective stages. The scales of the corresponding images are shown. (d) Drop height and freezing front height are plotted with respective time. The points highlighted in oranges represents instances of different stages. Corresponding contact angles are plotted.(e) The temperature profiles of the droplet during the whole process of spreading and freezing at different locations as shown in the <i>Stage – VI</i> are plotted. Inscribed plot represents the thermal profile of a sessile droplet dosed on a substrate at room temperature and then cooling is initiated.	20
2.3	Compares the experimental observations for non dimensional drop spreading radius R^* of a $6\mu l$, with the predicted theoretical results for different Stefan number, Ste , which is achieved by varying substrate temperatures (T_c) (a) for copper substrate. (b) corresponding contact angle measurements. (c) for aluminum substrate (d) for brass substrate . . .	31

2.4	(a)	The final shape formed by frozen droplet on copper substrate maintained at $-10^{\circ}C$, $-15^{\circ}C$ & $-20^{\circ}C$. The droplet height and corresponding freezing front of droplet during the entire spreading and freezing process for (b) copper substrate maintained at temperatures -10 , -15 , $-20^{\circ}C$. (c) copper,aluminum and brass maintained at fixed surface temperature of $-15^{\circ}C$. (d) freezing front of $6\mu l$ droplet on copper,aluminum and brass maintained at -10 , $-15^{\circ}C$. The start of freezing is set as the beginning of the freezing front.	35
3.1	(a)	Schematic diagram of water drop before and after freezing. h_s & h_ℓ represent the heights of solid and liquid drop heights respectively. θ_e is the contact angle made by the drop which initially maintained at temperature T_ℓ and dosed on a substrate at temperature T_{sub} (b) Experimental snapshots of liquid and solid water droplet with corresponding densities. Also shows the tip cone angle 2α . Scale bar represents $1mm$	41
3.2		Volumes during the final stages of the drop freezing for unfrozen drop, tip formation and dimple formation	43

3.3 (a) Parameters involved in theoretical modeling for symmetric drop having an initial contact angle θ_{av} ; h_i and h_w are the maximum height of the droplet in the solid and liquid phases, respectively; r and z are the radius and height of the solid-liquid interface at any time, respectively; h' is the height of the frozen part at any time, h_1 is the unfrozen part at that time, and h_2 is the final frozen part of the remaining height h_1 of the droplet. (b) Asymmetric drop having different initial contact angles, that is, the advancing contact angle θ_A and the receding contact angle θ_R with universal tip angle α . (c) Two superimposed symmetric droplets having initial contact angles of the asymmetric drop, that is, θ_A and θ_R ($\theta_A > \theta_R$). Based on these two different contact angles, we find two different corresponding heights of h_A and h_R , respectively, but due to the universality of the tip angle of drop freezing, we observe $\alpha_A = \alpha_R = \alpha$. (d) The theoretical basis of the two-triangle approach to predict asymmetric drop parameters: the approach indicates that $h_A < h_i < h_R$ with the assumption of $\alpha_A = \alpha_R = \alpha$ based on experimental observation. 45

3.4 (a)Ice h_s to water h_ℓ height ratio for symmetric and asymmetric drop. For the difference in contact angle $\leq 50^\circ$, this height ratio varies within 1.2 and 1.6. Within our experimental range, the two triangle approach suggests the height ratio of 1.2 while the new average contact angle approach suggest 1.5. (b)Ice h_s to water h_ℓ height ratio for symmetric and asymmetric drop as a function of gravitational field which can be represented by a non-dimensional Bond number. 51

3.5	(a) Asymmetric drop maximum height (h_s) prediction: We compare the two-triangle approach and the heat transfer model with our experimental results. Filled and empty circles represent the two triangle and heat transfer approaches, respectively. We investigate asymmetric drop freezing with four different metals for three different drop volumes. (b) Solid-liquid height ratio for different density ratios predicted by the two-triangle and average contact angle approach. The green line indicates the Tip cone angle for corresponding density ratios. The blue dashed line separates the plot at $\nu = 1$ representing the symmetric drop limitation. The images inscribed in the plot show the tip formation when $\nu < 1$ and the dimple formation when $\nu > 1$. The red dotted line highlights the height ratios predicted by both theoretical and experimental results and the respective tip angle for the case of water and paraffin wax	53
4.1	Schematic representation of the successive deposition of five droplets.	62
4.2	Schematic representation of the dosing sequence for each experimental condition, with ‘1’ indicating an open nozzle for liquid dosing and ‘0’ indicating no dosing.	64
4.3	(a) Shadowgraphic and (b) thermal images of the final column-ice structure for four experimental conditions $V_c f_v$, $V_c f_c$, $V_v f_v$, and $V_v f_c$	66
4.4	(a) Shadowgraphy images of each drop deposition and freezing front propagation (dotted red line) before the next drop along with corresponding time stamps. Graphs showing the progression of droplet height and the corresponding freezing front over time for the conditions (b) $V_c f_v$, (c) $V_c f_c$, (d) $V_v f_v$, and (e) $V_v f_c$	67

4.5	(a)Snapshots of thermal images of each drop deposition and solidification before the next drop along with corresponding time stamps. Locations at which the temperature profile are extracted are shown in final snapshot. Graphs illustrating the evolution of the thermal profile over time for the scenarios (b) $V_c f_v$, (c) $V_c f_c$, (d) $V_v f_v$, and (e) $V_v f_c$.	70
5.1	Ice structures printed using jet-based dosing technique	75
A.1	Phaseplots showing the variation in the spreading ratio ξ with respect to a) Reynolds (Re) and Stefan (Ste) numbers, b) Weber (We) and Stefan (Ste) numbers. The colour bar represents the different values of spreading ratio ξ	85

List of Symbols

2α	Tip cone angle, ($^{\circ}$)
κ	Thermal conductivity, (W/mK)
μ_l	Viscosity of liquid
C_p	Specific heat capacity, (J/KgK)
g	Gravity, (m/s^2)
L_f	Specific latent heat of fusion
t	Time, (s)
T_c	Surface temperature, ($^{\circ}C$)
T_m	Melting temperature, ($^{\circ}C$)

Chapter 1

ρ_i	Density of ice, (Kg/m^3)
ρ_w	Density of water, (Kg/m^3)
σ_{lg}	Surface tension of liquid-gas interface, (N/m)
σ_{sg}	Surface tension of solid-gas interface, (N/m)
σ_{sl}	Surface tension of solid-liquid interface, (N/m)
θ_d	Advancing (dynamic) contact angle, ($^{\circ}$)
θ_e	Equilibrium contact angle, ($^{\circ}$)

D_j	Liquid jet diameter, (m)
h_i	Height of frozen water droplet, (m)
h_w	Height of water droplet, (m)
m	Mass of the liquid
R_0	Initial spreading of the droplet, (m)
V_j	Liquid jet velocity, (m/s)

Chapter 2

ν	Solid-liquid density ratio
θ_A	Advancing contact angle, ($^\circ$)
θ_R	Receding contact angle, ($^\circ$)
θ_{av}	Average contact angle, ($^\circ$)
h_s	Height of solid droplet, (m)
h_ℓ	Height of liquid droplet, (m)

Chapter 1

Introduction

Water, in its three physical states, plays a vital role in the survival of life on our planet [1]. In particular, the exceptional freezing characteristics of water are considered to be ubiquitous, which is encountered in both nature and industry. The phenomenon of water freezing covers a wide range of applications, including, but not limited to, meteorology and climate change [2], spray freezing [3], and de-icing applications for process equipment [4], aircraft [5], and infrastructure [6]. The seemingly simple but complicated phenomenon of droplet freezing in the form of a spherical shape continues to puzzle both scientists and engineers alike. Given the significant relevance of this topic, numerous efforts have been made in recent decades to improve our understanding of the physics surrounding the solidification of droplets [7].

Drop freezing represents a complex series of steps that encompass various thermophysical events, including heat transfer and phase change processes [8]. The freezing sequence becomes even more complex when combined with wetting or spreading dynamics under the influence of external body forces. This dynamic process of spreading and freezing of water droplets has been the primary focus of studies involving icing on solid surfaces [9]. The freezing of drops on a solid surface has been widely investigated in recent years due to the negative impacts of ice accretion, which affects many natural processes [10–12].

The spreading dynamics of a droplet typically involves hydrodynamic motion at the three-phase contact line (TPCL), where the solid, liquid, and gas phases of the droplet meet. The equilibrium of forces acting on the TPCL occurs when the droplet is stationary. The movement of the TPCL, known as wettability, on a solid surface is influenced by various parameters of the liquid and solid, including surface tension, viscosity, kinetic energy, body forces, and interfacial energies, which collectively impede the movement of the TPCL. In cases of simultaneous freezing and spreading, heat transfer also significantly affects the arrest of TPCL [13]. This simultaneous process is critical in cryogenic 3D printing, a cutting-edge manufacturing technology with transformative potential across industries from aerospace to biomedical engineering [14].

Therefore, the aim of this thesis is to critically analyze and establish a rational understanding of the freezing mechanism of a deposited drop on a cold substrate. To achieve this, we conducted experimental investigations using high-speed and thermal imaging techniques. In addition, we develop mathematical models to quantify the spreading radius and height of the solidifying droplet.

1.1 Applications

Drop freezing, the process by which a liquid droplet transitions to a solid state, is a phenomenon of significant scientific interest and practical importance. Dynamics of drop freezing is one of the primary driving forces for various fields, ranging from science in nature to additive manufacturing. In nature, the need for a deeper understanding of the freezing dynamics has become more pressing because ice accretion can compromise the performance and safety of wind turbines [4], aircraft wings [5], and power transmission lines [6]. Therefore, several studies have been conducted to

investigate the complexities of icing phenomena for the development of anti-icing surfaces. In this endeavor, Schutzuus et al. [15] carried out an investigation to explore essential elements of the droplet freezing dynamics, such as the influence of surface roughness on nucleation, leading to a reduction in the contact area covered by TPCL [16].

Drop freezing also plays an important role in atmospheric science and climate research [17]. In clouds, the freezing of water droplets initiates the formation of ice crystals, which can influence precipitation patterns and cloud dynamics [18]. Understanding the freezing process of droplets in the atmosphere is crucial to improve weather prediction models and understanding the impact of clouds on climate change [19, 20]. A detailed investigation of the droplet solidification mechanism provides valuable information on the freezing process, which plays a crucial role in improving the effectiveness of food preservation [21], precise drug delivery systems [22], and the ceramic production sector [23]. Droplet freezing is a frequent phenomenon in spray freezing processes, which find application in a variety of engineering disciplines, including pharmaceuticals [24], atmospheric sciences [25], and artificial snowmaking [26], among other areas.

Another potential application of droplet freezing is cryogenic 3D printing, which can be further extended to biomedical / bioprinting applications [27]. For example, in the study by Tan et al. [28], a cryogenic 3D printing technique was used to print a composite hydrogel ink. In the study by Shahbazi et al. [29], the ability of the direction freezing in a liquid to generate porous materials has been investigated using the freeze drying process. 3D printing involves successive dosing of a liquid material in the form of layers. Although conventional 3D printing uses molten metal or polymer as the working fluid, Zhen et al. [30] used water as the working fluid to produce microscale ice structures. It is noteworthy to mention that during the 3D printing

process, the simultaneous spreading of drops along with freezing can be performed [14].

1.2 Aim of the present work

To accurately assess the wettability of droplets under freezing conditions, the deposited drop should be free of external body forces, which cannot be maintained in traditional impact-based drop deposition on a solid substrate. The impact of the drop on a solid surface distorted the drop contour, which makes it difficult to understand whether the drop shape change on a precooled substrate is due to the freezing or due to the impact forces. Given these complexities, an alternative approach in droplet generation is needed to more accurately quantify droplet wettability under freezing conditions. Therefore, this study uses a jet-based liquid dosing technique to improve the efficiency of droplet deposition [31, 32]. We examine the different stages of the freezing process of a droplet generated using the jet-based dosing method. Furthermore, we delve into the freezing dynamics to suggest successive droplet deposition in subzero environments. Based on the earlier discussion The specific objectives of this study are as follows:

- Investigate a jet-based technique to deposit a droplet and analyze the different stages involved in the freezing of a drop generated by the jet-based method.
- Develop a comprehensive theoretical model to determine the spreading of a freezing droplet.
- Analyze the parameters that determine the time delay for the freezing of a droplet.
- Characterize the universal behavior of a frozen water droplet.

- Investigate successive drop dosing using a jet-based method to obtain a column-like ice structure.

The background of the investigations is discussed in detail in the following sections. First, we consider the jet-based dosing method as an alternative method. Theoretical approaches that are currently available to determine the maximum spreading of the droplet while solidifying. Brief description of the stages involved in droplet freezing. Second, comment on the current understanding of the universal behavior of frozen droplets and what is missing. Finally, some background on 3D printing applications where successive drop deposition is studied.

1.3 Literature Review

1.3.1 Droplet spreading and freezing

This section summarizes the available literature related to the spreading and freezing of droplets. Many studies have focused on a droplet impact-based approach to investigate the spreading dynamics of a droplet as it solidifies [33]. Madejski [34] was probably the first to investigate the impact of droplets when a molten metal was deposited on a cold substrate. Spreading and solidification of the molten metal occur simultaneously. The impact of a droplet on a solid surface consists mainly of four stages, namely spreading, retraction, oscillations, and the final equilibrium state [35]. These stages behave differently when spreading and phase change is considered. In the study by Chang et al. [36] where a water drop is impacting a cold aluminum substrate, they observed that the maximum spreading factor of the TPCL increases with increasing height from which the droplet is released and decreases when the surface temperature is decreased.

The wettability of the surface also plays an important role in determining the hydrodynamic behavior of the droplet impact study [37]. For example, Zhang et al.

[38] performed the droplet impact study on cold hydrophobic surfaces with a contact angle (CA) of $90^\circ - 150^\circ$. They observed a transition from full rebound to full adhesion of the droplet to the substrate with decreasing drop temperature. The textured roughness of hydrophobic surfaces sometimes initiates ice nuclei before a full rebound of the droplet could occur, resulting in adhesion of the droplet to the substrate [39]. To fully understand the simultaneous spreading and freezing processes of a droplet on a cold substrate, relying solely on impact-based droplet freezing methods is not ideal. During the phenomenon of impact of the drop due to external body forces, such as inertial forces originating from impact velocities, the droplet undergoes complex shape changes, making it challenging to precisely characterize the mechanisms governing its spontaneous spreading and freezing [40, 41].

Therefore, a more gentle deposition method was utilized to understand the movement of the TPCL. In the research conducted by Schiaffino et al. [13], a series of micro droplets of microcrystalline wax were placed on the same material to study the transient motion of the TPCL. However, this step-by-step addition of tiny droplets led to forced spreading of the droplet. Ruiter et al. [42] implemented a pendant drop technique to deposit droplets, where the droplet is formed using a syringe, and observed arrest of TPCL in hexadecane droplets placed on a cold surface. They also noted stick-slip behavior on a glass surface. Jin et al. [31] proposed an innovative dosing approach using a jet-based method to create a drop. Ahmed et al. [32] compared the jet-based method with the pendant drop technique and found that the droplet volume affects the contact angle and dynamic wetting pressure. Although the jet-based dosing technique offers various benefits, to the best of my knowledge, there have been no studies examining the combined spreading and freezing behaviors of drops produced using this method. Therefore, this current research utilizes the jet-based approach to explore its implications for freezing and, by extension, for 3D printing applications.

Despite all the challenges to experimentally observed simultaneous spreading and freezing of the droplet, a comprehensive model is equally important, which depicts the physics behind it. In the study by Erickson et al.[43], an overall energy balance approach (OEB) is proposed, which is inspired by Madejski’s model. They performed an analysis of the isothermal condition by balancing the kinetic energy of the incoming energy (E_{in}) with the internal energy (E_{sys}), the surface energy (E_s), the work carried out due to viscous dissipation and boundary movement (W_{vd} & W_m), and the influence of body forces (E_g). This results in a first-order ODE as the governing equation. This model was able to predict the dynamic spreading rate of the TPCL with reasonable agreement. Therefore, the OEB approach has been applied to various conditions to determine wettability. Sumaiya et al. [44] investigated the effect of pressure on the hydrodynamically driven spreading of the water droplet using the OEB approach. Baldygin et al.[45] performed parabolic experiments to understand the effect of body forces on the spreading of the droplet. Therefore, the current study uses the OEB approach coupled with the effect of the solidification assumption from the Pasandideh model to determine the contact radius of the droplet. The OEB is shown below, where (E_T) is the energy due to heat transfer.

$$\frac{dE_{in}}{dt} = \frac{d}{dt}(E_{sys} + E_{se} + E_g) + \frac{d}{dt}(W_{vd} + W_{mv}) + \frac{dE_T}{dt} \quad (1.1)$$

1.3.2 Freezing dynamics of a water droplet

This section summarizes the current available literature on the different stages involved in the freezing of a water droplet. Fig. 1.1 illustrates the temperature transition for the entire water droplet freezing process. When a droplet is introduced to the cold substrate, the temperature of the droplet decreases depending on the latent heat release into the cold substrate [46]. The droplet temperature decreases below freezing temperature ($T_f = 0$) without any phase change, resulting in a phenomenon known

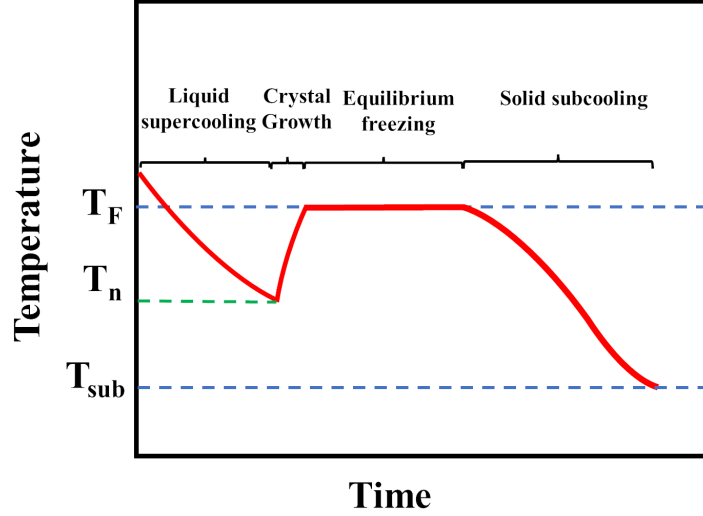


Figure 1.1: (a) Schematic representation of the temperature transition during the freezing of a droplet.

as the supercooling effect. When the drop reaches nucleation temperature (T_n), as shown in Fig. 1.1, crystallisation begins. Two primary types of nucleation are commonly identified: homogeneous nucleation [47], primarily resulting from evaporative cooling with the surrounding environment, and heterogeneous nucleation, which happens more frequently [48], typically induced by impurities or physical disruptions or when the droplet attains T_n . Once the nucleation is triggered, a sudden rise in temperature can be observed, this is because of rapid dendrite crystal growth into the bulk of droplet, this phenomena is also called as “recalescence” stage [11, 39, 47, 48]. Typically nucleation and recalescence occur in order of milliseconds, therefore these two stages are usually considered as one. The unfrozen liquid remains close to freezing temperature until the complete solid ice formation occurs. These temperature transition of water droplet freezing is well studied but for the case of jet-based droplet freezing it is still unknown.

Recalescence is followed by the propagation of solid ice formation, which can be represented by a moving solid-liquid interface. It is represented as solid subcooling in

Fig. 1.1. It is confirmed by several studies [49–51], the difference in density between the solid and liquid phases, i.e. water and ice, leads to a volumetric change, causing the freezing ice front to extend beyond the liquid-gas interface and resulting in the creation of what is referred to as a “pointy ice drop” [49, 50]. Despite the surface tension’s tendency to prevent pointed edges, the density contrast between the liquid and solid phases gives rise to a cusped singularity [8, 49]. Quantifying the tip cone angle can provide valuable information on specific liquid properties. For example, Boulogne et al. [52] observed minor deviations in the tip cone angle that can determine the purity of the liquid.

Regardless of the freezing parameters, the universal behavior of the tip-cone angle has been reported in multiple instances. It was first reported for the case of different contact angles and surface temperatures [53] for a symmetric droplet. Ismail et al. [54] later extended the universal behavior to asymmetric droplet freezing, since asymmetric droplet freezing is encountered more frequently in real-life applications than symmetric droplet freezing. The same phenomenon was also observed by Starostin et al. [8] when the droplet is frozen upside down. However, this does not comment on the morphology of the frozen water droplet, which is necessary when the universality of the frozen water droplet is considered.

1.3.3 Successive droplet freezing

This section provides an overview of the existing literature concerning the process of successive droplet deposition and freezing, also referred to as “pile-up”. The initial investigation of the pile-up phenomenon was carried out by Haferl et al. [55], who conducted a numerical analysis involving molten picoliter-sized liquid metals. Subsequently, the authors conducted experimental studies on the pile-up process using a droplet impact technique and noted that the shape of the final structure is sig-

nificantly influenced by impact velocities [56]. In recent years, numerous numerical investigations have drawn inspiration from Haferl’s research [57, 58]. For example, Li et al. [59] introduced a computational model to categorize bonding at each drop interface, including classifications such as no bonding, partial bonding, ideal bonding, and excessive bonding. However, to the best of my knowledge, there is a lack of experimental data addressing the bonding at drop interfaces. The advancement in cryogenic 3D printing applications has sparked renewed interest in “ice printing” [14]. Jin et al. [60] were probably the first to investigate successive freezing of water droplets, where three droplets were deposited on an ice surface. Their findings highlighted the significant role that initial droplet spreading and height played in total freezing time and height of the structure. Zhen et al. [30] demonstrated the creation of 3D printed ice structures, a concept also explored in the study by Garg et al. [61]. While these studies are crucial for elucidating the fundamentals of 3D ice printing using picoliter volume drops, their practical applicability may be limited.

1.4 Thesis Outline

This thesis comprehensively explores the dynamics of droplet spreading and freezing, particularly focusing on a jet-based deposition technique. It is structured as follows:

In Chapter 2, we discuss in detail the stages of jet-based droplet deposition on a pre-cooled substrate. This chapter uses thermal imaging and analysis to improve our understanding of the freezing process. A comprehensive theoretical model based on the OEB approach is developed to predict the spreading rate of the droplet as a function of nondimensional numbers. The theoretically obtained spreading rate was validated using the experimental findings. In the later section of the chapter, we analyzed the experimental parameters, such as the surface temperature and thermal properties of the substrate on the freezing delay.

In Chapter 3, the concept of universality for the solid-liquid height of the water droplet is presented. A novel two-triangle approach was proposed to determine the height of the frozen drop. This approach not only offers insight into predicting the size of solidified deposited material but does so irrespective of the body forces acting on the droplet. Finally, a comparison was made between the two-triangle model and other available models.

In Chapter 4, we investigated the use of jet-based technique in successive droplet freezing to create column-like ice structures. It presents four distinct cases, varying in droplet volume and dosing frequency. The chapter uses shadow photography to analyze the freezing dynamics for column structure. The current OEB model was extended to theoretically predict the droplet height and freezing front propagation. In the later section, we presented the thermal imaging results to investigate the effect of heat accumulation between each droplet.

Chapter 5 concludes the thesis by summarizing the analysis of all chapters and underlining the key findings. This chapter also addresses topics that remain unexplored within the thesis, offering suggestions for future research directions.

Chapter 2

Freezing of a Spreading Droplet

2.1 Abstract

Here, we present a theoretical and experimental study of simultaneous spreading and freezing of sessile droplets on a precooled substrate. Although many studies have explored the freezing dynamics of subcooled water droplets on a solid substrate, a thorough investigation on the freezing of a room temperature droplet while spreading on a precooled solid substrate is yet to be addressed. In this study, we developed a theoretical model based on the overall energy balance equation to quantify the transient variation of the moving three-phase contact line of a spreading droplet at room temperature before deposition on a precooled solid substrate. The presented mathematical model also accounts for a jet-based deposition technique, which facilitates the precise deposition of a droplet on a precooled substrate, the heat transfer between the drop and substrate, viscous dissipation, surface and interfacial energies, and the kinetic energy of the incoming jet during the jet-based deposition. By validating the theoretical model with the experimental observations, we demonstrated that the proposed theoretical model could successfully predict experimental observations. Through theoretical analysis and extensive experimental investigations, we formulated a rational understanding that allowed us to comment on the effect of all the governing dimensionless numbers such as the Weber, Reynolds, Bond, Stefan, and Peclet numbers on the maximum spreading of a droplet on a precooled substrate. In

addition to explaining the physics of the transient variation of a three-phase contact line, the role of a substrate temperature on controlling the dynamics of the freezing front, the freezing time, and the overall height of the frozen drop is also presented.

2.2 Introduction

The freezing of water droplets is a complex and natural phenomenon that has a wide range of applications. Solid surfaces can be affected by the freezing and accumulation of frozen droplets, which can have an impact on both industrial processes and our daily activities. Smooth flight operations of aircraft [5], wind turbines [4], and power transmission cables [6] can be disrupted by freezing droplets on their surfaces. In addition, the freezing of liquids is a crucial process, which can dictate the fate of 3D printed processes at low temperatures, such as bioprinted objects [62], as well as the quality of the thermal spray coating [3]. In order to fully comprehend the effect of drop freezing, developing a rational understanding of the influence of drop deposition and subsequent wetting dynamics coupled with heat transfer terms is crucial. Another aspect to consider in relation to the applications mentioned above is the drop generation through jetting on subcooled substrates.

Since the pioneering work of Madjeski [34], where the overall energy balance (OEB) approach was proposed to determine the maximum flattening of an impinging molten drop, many studies have been devoted to understanding the solidification mechanism of a droplet impinging on a subcooled surface [3, 63, 64]. The impact of a droplet on a solid surface consists mainly of four stages, namely spreading, retraction, oscillations, and the final equilibrium state [35]. Thievenaz et al. [65] mentioned that these stages act differently when spreading and phase transition is considered, and observed a delay between spreading and retraction of the three-phase contact line (TPCL). Later on, for a supercooled droplet impacting on a cold hydrophobic surface, Zhang et al. [38] observed a transition from full rebound to full adhesion of the droplet to the sub-

strate, with decreasing temperature. It is noteworthy to mention that the thickness of the thermal spray coating layer at low temperatures is greatly influenced by the wetting dynamics of an impacting drop on a colder substrate [66].

To fully understand the simultaneous spreading and freezing processes drop generation through jetting on a cold substrate, relying solely on impact-based droplet freezing methods is not ideal. During the drop impact phenomenon due to external body forces, such as inertial forces originating from impact velocities, the droplet undergoes complex shape changes, making it challenging to precisely characterize the mechanisms governing their spontaneous spreading and freezing [40, 41]. Therefore, to accurately examine the correlation between the wetting and freezing kinetics of the droplet, it is crucial to employ a deposition method that minimizes the effects of these external forces. Gentle deposition mechanisms, such as the use of pipettes [47, 67, 68] or syringes [8, 44, 49], have been adopted to investigate the freezing dynamics of sessile droplets more effectively.

Pendant droplet deposition, although widely used, is not without limitations due to the influence of body forces. Kwon et al. [69] and Ahmed et al. [32] observed that removal of the needle immediately after droplet deposition can introduce capillary waves and a water hammer effect, leading to forced spreading of the droplet. This phenomenon can compromise the accuracy of the experimental findings. For example, Ruiter et al. [42] reported the arrest of TPCL in hexadecane droplets deposited on a cold substrate using the pendant drop technique. Specifically, on a glass substrate, stick-slip behavior was observed, which was characterized by the pinning and depinning of the TPCL. In response to these challenges, Jin et al. [31] introduced a novel dosing technique that involves the use of jet-based dosing instead of the pendant drop technique, also termed liquid needle dosing [45]. This method aims to mitigate the impact of external forces on droplet spreading and freezing, which also appropriately

mimics the practical applications such as 3D printing and spray painting. Ahmed et al. [32] conducted a comparative study between jet-based dosing and the traditional pendant drop technique, revealing that the droplet volume significantly affects the contact angle and the dynamic wetting pressure. Furthermore, Baldygin et al. [45] explored the effectiveness of jet-based dosing under reduced gravity conditions through a series of parabolic flight experiments designed to simulate a low-gravity environment. However, to our knowledge, to date there has been no investigation of the freezing dynamics of a droplet on a subcooled substrate deposited by the jet-based deposition technique. Furthermore, a comprehensive theoretical model that predicts the morphological evolution of a water droplet during spreading on a subcooled substrate, along with the simultaneous freezing dynamics, is also missing from the literature.

Therefore, to address the aforementioned knowledge gap, in this study, we perform a thorough experimental and theoretical investigation on the solidification dynamics while spreading on a subcooled substrate. To achieve this, a jet-based dosing technique is employed to deposit droplets with high precision. In order to observe the effect of substrate properties on the dynamics of freezing and spreading, substrates with varying thermal conductivity were used. Further, we carefully scrutinize the different stages involved in the jet-based dosing process, while the temperature profiles of a solidified drop, captured from thermal camera, are analyzed to understand the heat transfer process during droplet freezing. Furthermore, a theoretical model is developed based on the overall energy balance approach, and the theory is validated with our experimental observation. Finally, the dynamics of freezing is investigated to identify the factors that affect the freezing delay and rate.

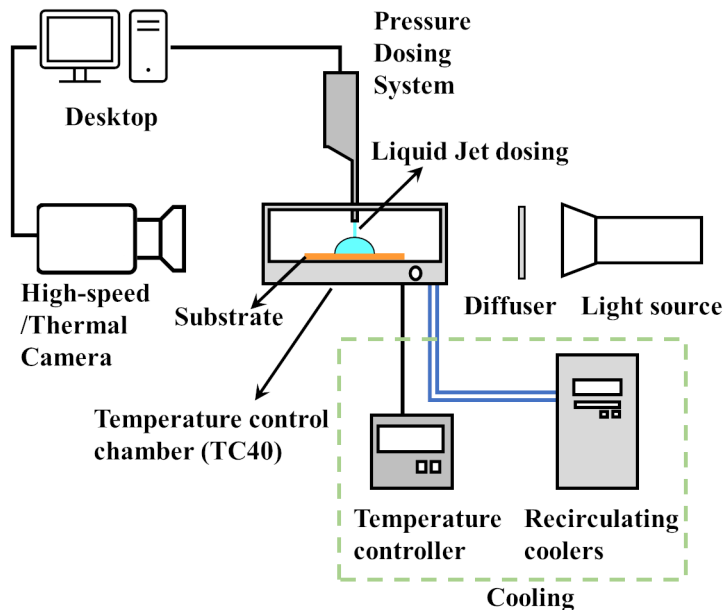


Figure 2.1: Schematic diagram of the experimental setup.

2.3 Experimental description

2.3.1 Materials and methods

The schematic of the experimental apparatus used for the current research study is illustrated in Fig.2.1. The essential parts of the experimental arrangement include a dosing unit and a temperature-regulating system to maintain the substrate temperature. High-speed imaging is used to capture the underlining phenomena.

Experiments are carried out using a goniometer (DSA100, KRÜSS). A temperature control chamber (TC40, KRÜSS) was used to regulate and maintain the environmental conditions during the experiments. This chamber was equipped with recirculating coolers (F12, JULABO) and a precise temperature controller (KRÜSS) to ensure accurate temperature control. Relative humidity (RH) within the TC40 temperature control chamber was meticulously regulated using silica desiccants (10 gram silica gel packets, LotFancy). These packets can absorb 40% of their weight in water vapor. Desiccants were placed within the chamber to achieve and maintain an RH below

10% for the duration of each experiment.

To generate a drop using the jet-based dosing technique, a pressure dosing system (DO3252, KRÜSS) was used. The diameter of the jet D_j is $\sim 0.1\text{mm}$. We meticulously maintained the flow rate at $15 \pm 2\mu\text{ls}^{-1}$, a rate that ensures a continuous jet that would neither break up prematurely nor cause splashing upon contact with the substrate. The substrates used in this study were obtained from McMaster-CARR and had a mirror-like finish on one side. Different substrates with varying thermal conductivity's, including copper, aluminum, and brass, were utilized. Because all of the substrates were metallic, they exhibited hydrophilic properties. The physical properties of these substrates are summarized in Table 2.1. As part of the cleaning process, the substrates were carefully subjected to flame treatment following the steps mentioned in [45]. The use of degasified DI water in this study helped prevent the trapping of air in the droplet. Consequently, there was a reduced probability of air bubbles being trapped during the freezing process, which could potentially affect heat conduction [70].

Shadowgraphic and thermal images were recorded using a high-speed camera (FAST-CAM NOVA S9, Photron) and an infrared thermal camera (A6700, FLIR Systems), respectively. The high-speed camera captured the entire freezing process at a frame rate of 1000 Hz, allowing for detailed analysis of the spreading and freezing stages. In all experiments, a resolution of 640×465 and a shutter speed of $1/7000$ are used. Photron FASTCAM Viewer software (*PFV4*, Photron) was used to modify and record high-speed images. A needle of diameter 0.52mm was recorded for calibration purposes. Subsequently, the high-speed camera footage was analyzed using Image-Pro V10 (Media cybernatics) to extract relevant parameters and characterize the different stages of sessile droplet freezing. However, the thermal camera captured the temperature of the droplet surface at a rate of 400 Hz. A resolution of 160×128 was

achieved by employing a lens assembly with a focal length of 25mm . The infrared camera provides a non-intrusive method for recording the temporal evolution of the temperature profiles of a freezing droplet. The proprietary software (FLIR Research Studio, FLIR Systems) was used to monitor and analyze the thermal profiles. It is noteworthy to mention that the thermal effusivity (which is related to the exchange of heat from a surface) of the water shown in Table 2.1 is considered when measuring the temperature profiles of the freezing droplet.

Table 2.1: Physical properties of the substrates and the liquid used for current study

Material	Density (Kg m^{-3})	Thermal Conductivity ($\text{W m}^{-1} \text{K}^{-1}$)	Specific Heat ($\text{J Kg}^{-1} \text{K}^{-1}$)	Thermal Effusivity ($\text{J s}^{-\frac{1}{2}} \text{m}^{-2} \text{K}^{-1}$)
Copper	8960	398	385	37053
Aluminum	2700	218	897	22977
Brass	8530	109	380	18796
Water	1000	0.58	4182	1557
Ice	917	2.18	2100	2048

2.3.2 Uncertainty analysis

Measurement uncertainties are categorized into random and systematic types. Even with careful adherence to experimental procedures, the possibility of random uncertainties remains. One source of uncertainty lies in the precision or accuracy of measurement devices, such as the flow rate of the liquid jet, which exhibits an error of $15 \pm 2 \mu\text{s}^{-1}$. This variation results in non-repeatable volumes for each drop, although it does not significantly impact the current study due to the Bond number being less than 1. Moreover, during image processing, uncertainties arise, notably ADVANCE software used for measuring contact angles, which shows an error of $\pm 2^\circ$. Similarly, Image-Pro software, employed to determine droplet dynamics, may be subject to precision errors or potential human errors during calibration. Furthermore,

human errors may occur during substrate flame treatment. Inconsistencies in maintaining precise surface temperatures within the temperature control chamber, with an error of $\pm 3^\circ C$, also contribute to uncertainties. Parallax inaccuracies caused by the angle at which high-speed cameras are viewed. Variations in the environment inside the chamber, where the relative humidity is kept around $10\% \pm 2\%$, also contribute to raising uncertainties. To reduce these random uncertainties, multiple measurements are taken, and averages are computed to report error bars, represented as standard deviations.

2.4 Results and Discussion

2.4.1 Jet-based drop deposition

Fig. 2.2 (a) illustrates the distinct stages involved in spreading and freezing a water drop deposited through jetting and the corresponding experimental snapshots are shown in Fig. 2.2 (b). *Stage – I* is the liquid jet of diameter D_j impinging on the substrate with a velocity V_j and forms a splat-shaped structure. The time is set to zero for *Stage – I*. The diameter of the jet $D_j = 0.1mm$ is significantly smaller compared to the generated drop, reducing the influence of the incoming kinetic energy on the measured contact angles [45]. To achieve a continuous jet, the jet flow rate was set at $15 \pm 2\mu l s^{-1}$ outwards, as depicted in *Stage – II*, until the incoming jet flow is seized. For the current study, $6\mu l$ droplets are generated that are below the capillary length of the water ($\lambda_c = 2.7mm$), signifying the influence of surface tension during drop growth. It is important to note that there is a minimum volume threshold of $2\mu l$ below which the influence of incoming jet kinetic energy still exists [32]. Finally, the drop attains equilibrium, which is considered to be the maximum wetting of the droplet.

Once equilibrium is reached (*Stage – III*), the freezing phenomenon begins with

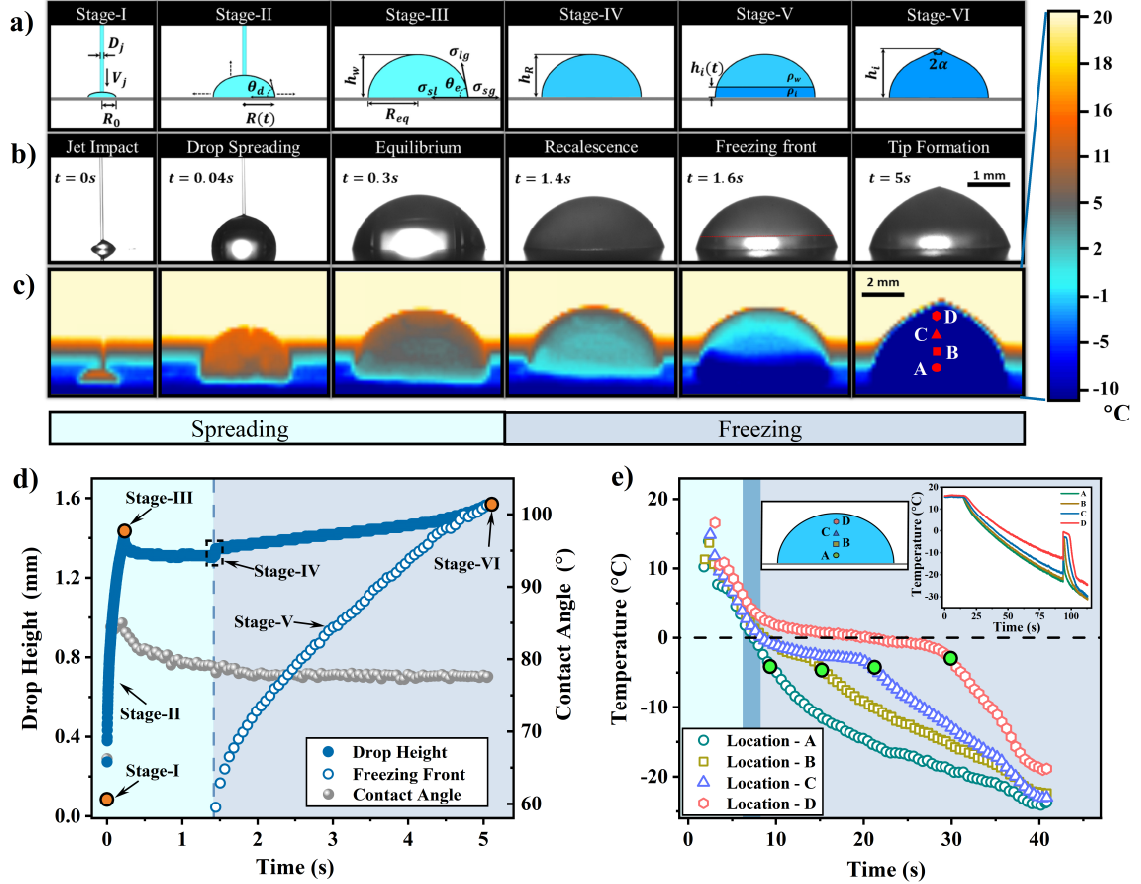


Figure 2.2: (a) Schematic representation of the stages involved in jet-based dosing system. Also represents the nomenclature used for current study. (b) and (c) shows the shadow graphic and thermal experimental images for the respective stages. The scales of the corresponding images are shown. (d) Drop height and freezing front height are plotted with respective time. The points highlighted in oranges represents instances of different stages. Corresponding contact angles are plotted. (e) The temperature profiles of the droplet during the whole process of spreading and freezing at different locations as shown in the *Stage – VI* are plotted. Incribed plot represents the thermal profile of a sessile droplet dosed on a substrate at room temperature and then cooling is initiated.

heterogeneous nucleation near the liquid-solid interface. We observed a noticeable delay before the nucleation occurred, and this has been discussed in detail in the following sections. Within a time frame of several hundred milliseconds, depending on the volume, the bulk liquid undergoes rapid solidification, resulting in the formation of a dendritic ice-shaped structure [48]. This crystallization in the bulk liquid increases the liquid temperature, which is termed as the “recalescence” stage (*Stage – IV*). It should be mentioned that a thin circumferential ice layer formation has been reported immediately after nucleation that initially propagates radially and leads to rapid dendritic ice (recalescence stage) filling the droplet [48]. The dynamics of the recalescence stages depends on the stability of the solid-liquid interface of this thin ice layer [71, 72]. However, this thin initial ice layer occurs right after nucleation, following a very fast dynamics with $\sim O(1)\mu s$. It is worth mentioning that to capture the entire freezing phenomenon, the optimized frame rate of $1000Hz$ does not capture the first stage nucleation. Therefore, although nucleation and its influence on freezing delays have been discussed in this study, the event related to first stage nucleation has not been experimentally measured. Instead, the start of the recalescence stage is considered the occurrence of nucleation. The recalescence stage can be distinguished by observing the change in transparency inside the drop [47], which is represented by Fig. 2.2. (b), *Stage – IV* at time $t = 1.4s$.

Additional release of heat from the drop that results in freezing of the remaining water. This is observed in the form of an isothermal freezing front that propagates normally to the substrate as shown in *Stage – V*. The freezing front serves as a visual representation of phase transition, providing valuable insight into the kinetics of freezing and the interplay between temperature gradients and material properties. A pointy tip formation is observed at the end of the freezing (*Stage – VI*) due to the density difference in the solid and liquid phase of the drop [50]. The angle formed at the tip, also known as tip cone angle (2α), is constant for a fixed density ratio. For

instance liquid to solid density ratio (ν) of a frozen water droplet is 0.917 for which the corresponding tip angle is $2\alpha = 130^\circ$ [53, 54, 73].

The temporal evolution of the droplet height and the freezing front can be used to represent the entire process of growth and freezing of the water drop, as shown in Fig. 2.2 (d). A gradual increase in height is observed during mass addition until the end of dosing (*Stage – II*). While the jet is actively generating the drop, cohesion causes the drop to climb toward the jet. Subsequently, when the jet ceases, the droplet’s height decreases slightly until it reaches equilibrium *Stage – III* of Fig. 2.2 (d). The drop remains in equilibrium until the beginning of the recalescence stage (*Stage – IV*), where a sudden increase in the height of the drop is observed, which is caused by the expansion of the volume of the ice-water mixture [74]. This is followed by the propagation of the freezing front (*Stage – V*), leading to the formation of the tip (*Stage – VI*). The corresponding contact angle (CA) evolution throughout this transient process is illustrated in Fig. 2.2 (d). The contact angle plays a pivotal role in determining the freezing time of a droplet on a solid surface, as it directly influences the droplet’s interaction with the substrate[67, 75]. Once the freezing process commences, the CA becomes fixed due to the pinning of the TPCL.

2.4.2 Temperature profiles

To better elucidate the different stages associated with the spreading of a drop, deposited by the jet-based deposition technique, on a subcooled substrate, we have extended our scope to thermal imaging. We used an infrared (IR) thermal camera to capture the temperature profiles of the droplets. One of the advantages of using an IR thermal camera is its non-invasive measurement capabilities. Therefore, the temperatures obtained are from the external surface of the drop. Fig. 2.2 (c) shows snapshots of various stages of a $25\mu\text{l}$ drop deposited on a precooled copper surface

maintained at -15°C . A larger drop volume is used so that the temperature gradients inside the drop during each phase are clearly visible. The liquid at room temperature is deposited on a precooled substrate, and hence the temperature of the liquid gradually decreases.

Heat transfer through conduction from the cooled surface plays a significant role in the freezing process, overshadowing the effects of convection and radiation that might occur at the liquid-gas interface. This predominance of conduction is attributed to direct thermal contact between the droplet and the solid surface, facilitating efficient heat dissipation. Although the temperature difference between the liquid-gas interface and the surrounding medium can create density gradients [46], the current study assumes that these effects are negligible. The heat flux through the solid-liquid interface is higher compared to the liquid-gas interface when the effect of evaporative cooling is ignored [71, 72]. Hence, heterogeneous nucleation is a common occurrence observed in the experiments conducted in the present study.

The thermal profile of the freezing droplet is meticulously observed by measuring the temperatures at four distinct locations (A, B, C, and D denoted in the inset of Fig. 2.2 (e)). The temporal progression of the temperatures at these four different locations of the droplet is depicted in Fig. 2.2 (e). Initially, the liquid was at room temperature prior to dosing. The graph shows that as the droplet grows, the temperature at each measurement location decreases uniformly until it reaches equilibrium at *Stage – IV*. This uniform rate of temperature decrease is maintained by consistent heat transfer through conduction from the cooled surface, assuming that the substrate temperature was marginally changed. This gradual cooling process is momentarily disrupted by the recalescence stage, which precedes the droplet reaching subcooling temperatures. This phenomenon is attributed to the release of latent heat during the exothermic crystallization process, which occurs in the form of dendritic ice within

the droplet[68].

To investigate the impact of supercooling on droplet freezing, we deposited a sessile droplet on a copper surface at ambient temperature and then gradually lowered the substrate temperature. The temperature profile of the entire droplet freezing process from the moment the drop is deposited at room temperature until the final tip formation is plotted in the inset graph of Fig. 2.2 (e). A notable supercooling effect was observed, with temperatures dropping as low as $-25^{\circ}C$ without phase change. During the onset of recalescence, the drop experienced a rapid increase in temperature that reached close to $0^{\circ}C$. Subsequently, the temperature decreased as the freezing front propagated. However, in the current study for jet-based dosing, recalescence occurred before the drop temperatures could reach subzero temperatures. Therefore, the temperature of the unfrozen liquid remained close to $0^{\circ}C$ after recalescence, and no rapid increase was observed. It is noteworthy to mention that the onset of the recalescence stage is highly probabilistic[68].

Further investigation of Fig. 2.2 (e) reveals that during jet-based dosing, the supercooling effect cannot be observed with the minimum time scale of experimental observation considered here. The reason behind the absence of the supercooling effect can be attributed to competition between heat transfer and mass addition. This is different from the freezing of a droplet with pendant drop deposition, where the entire drop spreads instantaneously. Here, the entire drop deposition is $\sim O(s)$ where the instantaneous spreading is $\sim O(ms)$. In our operating conditions, heat release during the recalescence stage for jet-based dosing is observed as a change in the slope of the temperature profile, as shown in Fig. 2.2 (e), where the temperature decrease is slowed due to latent heat release. This delimitation of a noticeable change in temperature gradient is noticeable for all locations except location A, which is very close to the substrate, leading to a freezing front to reach that location first. The tempera-

ture of the liquid phase remains close to $0^{\circ}C$ until the liquid has fully solidified. The green-filled circles highlighted in Fig. 2.2(e) represent the time at which the freezing front reaches the specified location. A temperature gradient develops within the growing front which can be observed in the figure. The cooling rate again matches the initial rate once the freezing front reaches each location. At the end in *Stage – VI* after the formation of the tip, the temperature of the drop reaches equilibrium. The orientation of the final tip cone is said to be influenced by the direction of heat flux within the solid surface below [8].

2.4.3 Theoretical Model

The process of freezing a droplet while spreading is a complicated problem because it involves a three-phase contact line (TPCL) that is in motion, along with simultaneous transfer of heat. When the system is at room temperature, the spreading of a drop of water depends on inertial, viscous, and capillary forces [44]. However, when the substrate is lower than the freezing temperature of the drop, heat transfer between the drop and the substrate restricts the movement of TPCL, resulting in reduced wetting [42]. To predict the movement of TPCL while the drop is freezing, in this study, we developed a mathematical model based on the overall energy balance approach (OEB), coupled with aspects of heat transfer.

The OEB approach proposed by Madejski [34] equates the incoming energy of the impinging drop with the surface energy, the viscous dissipation, and the change in the kinetic energy of the solid layer. On the other hand, this classical model made several assumptions. Therefore, many studies have found improvements in OEB suggested by Madejski [76]. The study by Pasandideh et al. [77] simplified the OEB to obtain a governing equation that can determine the maximum flattening of a molten drop on a cold substrate. Erickson et al. [43] was the first to employ OEB to determine the

transient spreading of the water droplet where the influence of gravitational energy and baldygin et al. [45] extended the same model with appropriate assumption for reduced gravity droplet spreading.

The current study followed a similar approach to elucidate the dynamics of droplet spreading, incorporating the continuous addition of mass until equilibrium was reached. Throughout this process, the continuous flow of liquid into the system acts as the main driving force for the droplet spreading. In the context of the jet-based droplet deposition technique, the energy of the impinging jet (E_{in}) is transformed into surface energy(E_{SE}), gravitational energy(E_g), and accounting for the resistance from viscous dissipation (W_{vd}) within the spreading droplet. Since the droplet is dosed on a precooled surface, the energy due to heat transfer(E_T) must be considered [43–45]:

$$\frac{dE_{in}}{dt} = \frac{d}{dt}(E_{se} + E_g) + \frac{d}{dt}(W_{vd} + W_{mv}) + \frac{dE_T}{dt} \quad (2.1)$$

Incoming Energy

The kinetic energy of the incoming jet is given by:

$$\frac{dE_{in}}{dt} = \left(\frac{V_j^2}{2} \right) \frac{dm}{dt} \quad (2.2)$$

where, m – mass of liquid, V_j – jet velocity.

Surface energy of the Droplet

The total surface energy of the system can be defined by considering the surface energies of the three interfacial phases, i.e. solid-liquid, liquid-gas, and solid-gas.

$$\frac{dE_s}{dt} = (\sigma_{sl} - \sigma_{sg}) \left[2\pi R \frac{dR}{dt} \right] + \sigma_{lg} \left[4\pi h(\theta_d) R \frac{dR}{dt} + 2\pi R^2 \frac{dh(\theta_d)}{dt} \right] \quad (2.3)$$

where, $h(\theta_d) = \frac{1-\cos(\theta_d)}{\sin^2(\theta_d)}$, $\sigma_{sl}, \sigma_{lg}, \sigma_{sg}$ are surface tension at solid-liquid, liquid-gas and solid-gas.

Gravitational Energy

For infinitesimal increases in mass Δm and if the change in height of the center of gravity is Δz , then the equation representing the gravitational potential energy will be

$$\frac{dE_g}{dt} = g \left[m \left(\frac{3}{4} f(\theta_d) \frac{dR}{dt} + \frac{3R}{4} \frac{df(\theta_d)}{dt} \right) + \frac{3R}{4} f(\theta_d) \frac{dm}{dt} \right] \quad (2.4)$$

where, $f(\theta_d) = \frac{2-2\cos\theta_d+\sin^2\theta_d}{\sin\theta_d(2+\cos\theta_d)}$ and $m = m_0 + \int \frac{dm}{dt} dt$ where m_0 is the initial mass of the system given by $m_o = \frac{\pi\rho_l R_o^3(1-\cos\theta_d)^2(2+\cos\theta_d)}{3\sin^3\theta_d}$

Viscous Dissipation

Based on equilibrium contact angles θ_e , two models have been proposed to determine viscous dissipation work, that is, the lubrication approximation and the boundary layer approximation. There are studies that compare both approaches [44]. The lubrication approximation is more accurate when θ_e is less than 90° , while the boundary layer approximation is more appropriate when θ_e is greater than 90° [44, 45]. Given that hydrophilic metallic substrates were utilized in the present investigation, it was deemed suitable to use the lubrication approximation theory [78]. The calculation of the viscous dissipation work using the lubrication approximation is as follows:

$$\frac{dW_{vd}}{dt} = 6\pi\mu_l n(\epsilon^{-1}) \frac{R}{\theta_d} \left(\frac{dR}{dt} \right)^2 \quad (2.5)$$

where, μ_l is the viscosity of water, ϵ is the ratio between microscopic L_δ and macroscopic cutoff length L (L_δ may vary between $1\mu m$ & $5\mu m$ and L can be defined as the characteristic length scale of the drop). In this research, the impact of medium viscosity (W_{mv}) is considered negligible, given that the medium being referred to is

air. Please refer to the appropriate literature for calculations related to the work performed by the viscosity of the medium in situations involving a viscous medium[43–45].

Energy due to heat transfer

The effect of heat transfer on the spreading dynamics of the droplet is a complex problem that requires understanding of several aspects. For simplicity, we make the assumption that the effect of heat transfer can be determined by considering that a thin ice layer starts to propagate as soon as *Stage – I* and the kinetic energy stored in this ice layer is lost once the TPCL is arrested or in equilibrium. We have followed the Pasandideh approach [79] to determine the loss of kinetic energy of the ice layer. The effect of solidification is determined by the difference in the initial and final kinetic energy of the thin solid/ice layer formed during the spreading. Let the thickness and radius of the ice layer be h_{io} and r_i , respectively, and let the initial velocity of the ice layer be the same as the jet velocity V_j . Therefore, the energy due to heat transfer is given by:

$$E_T = (\rho_i \pi r_i^2 h_{io}) \left(\frac{V_j^2}{2} \right) \quad (2.6)$$

Here, h_{io} is given by the one-dimensional Stefan problem [7]. However, it is reasonable to consider $r_i \sim R/2$ [77]. Considering the fact that the droplet grows, differentiating eq. 2.6, we can obtain the rate of energy stored in the ice layer as it grows radially. we get:

$$\frac{dE_T}{dt} = \frac{\pi}{4} \rho_i v_j^2 h_{io} R \frac{dR}{dt} \quad (2.7)$$

Inserting the energy terms (2–7) in eq. 2.1 we get the combined governing equation for the spreading of freezing droplets is given by the following:

$$6\pi\mu_d \ln(\epsilon^{-1}) \frac{R}{\theta_d} \left(\frac{dR}{dt} \right)^2 + \left[2\pi R \sigma_{dm} [2h(\theta_d) - \cos \theta_e] + \frac{3mg}{4} f(\theta_d) + \frac{\pi}{4} \rho_i v_j^2 h_{io} R \right] \frac{dR}{dt} + \left[\frac{3R}{4} g f(\theta_d) - \left(\frac{V_j^2}{2} \right) \right] \frac{dm}{dt} = 0 \quad (2.8)$$

By considering the appropriate time, length, and temperature scale, the final non-dimensional governing equation is given by:

$$\frac{6 \ln(\epsilon^{-1}) R^*}{\theta_d Re} \left(\frac{dR^*}{dt^*} \right)^2 + \left[\frac{4R^*}{We} [2h(\theta_d) - \cos \theta_e] + \frac{f(\theta_d) G(\theta_d) Bo}{24 We} (R_o^*)^3 + \frac{f(\theta_d) t^* Bo}{4 We} + \rho^* R^* \sqrt{2 \frac{Ste}{Pe} t_o^*} \right] \frac{dR^*}{dt^*} + \left[\frac{3R^* Bo}{4 We} f(\theta_d) - 1 \right] = 0 \quad (2.9)$$

Here, the characteristic length, time, and temperature are considered as D_j , $\frac{D_j}{V_j}$ & T_m respectively. Where $R^* = \frac{R}{D_j/2}$, $t^* = t \frac{V_j}{D_j}$, $Re = \frac{\rho_w V_j D_j}{\mu_i}$, $We = \frac{\rho_w V_j^2 D_j}{\sigma_{1g}}$, $Bo = \frac{\rho_w g D_j^2}{\sigma_{1g}}$, $Ste = \frac{C_p \Delta T}{L_f} (\Delta T = T_m - T_c)$, $Pe = \frac{\rho_w C_p V_j D_j}{k}$. The hydrodynamic spreading of a droplet on a precooled substrate is theoretically modeled by solving nonlinear ordinary differential equations 2.8 or 2.9. Because of its non-linearity, they are strongly dependent on the initial conditions. The initial condition for the current study can be obtained by determining the diameter of the initial splat formed in *Stage - I* when the jet impacts the substrate. The maximum spreading of the splat resulting from the initial impact of the jet can be non-dimensionalization and can be represented as the initial spreading ratio, $\xi = \frac{D_o}{D_j} = \frac{R_o}{R_j}$. We can assume that at the first instant, the splat-shaped drop spreading is obtained with a drop volume equivalent to the initial jet volume immediately before impact. The detailed derivation to determine the initial condition for a splat shape drop generated by jet impact at room temperature is given in [45]. The influence of heat transfer can be obtained by considering eq. 2.6. The initial spreading ratio ($\xi = \frac{D_o}{D_j}$) for a jet-based dosing on a precooled substrate can be:

$$\xi^3 \left[\frac{9 \ln(\epsilon^{-1})}{32 \theta_d} \right] \frac{We}{Re} + \xi^2 \left[\frac{(1 - \cos \theta_e)}{4} + \frac{We}{8} \sqrt{\frac{3 Ste}{4 Pe}} \right] - \frac{Kh_j}{8} We = 0 \quad (2.10)$$

The ordinary differential equation is solved numerically using the Runge-Kutta (RK-4) method with appropriate initial conditions, such as the radius of the drop $R_o^* = \xi$ during the initial impact of the jet on the substrate. Matlab software *R2023* was used to solve the first-order ordinary differential equation. Furthermore, the values of dynamic advancing/dynamic contact angles θ_d and equilibrium contact angles θ_e are kept fixed for specific substrate and temperature conditions and are subsequently obtained from experiments. During the solution of the equation, the θ_d, θ_e , volume flux, and time until the jet nozzle close are known from the experiments. It is worth mentioning that a spherical cap assumption has been considered for the current theoretical model.

2.4.4 Droplet spreading

The importance of understanding the spreading / wetting dynamics of a droplet on a solid surface is rather indispensable. Employing jet-based dosing can be an improved technique for studying the displacement of TPCL on a solid surface, which creates the droplet by continuously adding mass. A well-accepted spherical cap assumption is considered, which helps us to quantify the movement of the TPCL by measuring the transient motion of the base radius (R) and the dynamic contact angle (θ_d) of the drop. To investigate this, we experimentally measured the transient growth of (R) and compared it with the results theoretically obtained. We performed a comparative analysis between experimental and theoretical results, as shown in Fig. 2.3 for the nondimensional base radius R^* of a droplet with respect to the nondimensional time t^* on three different substrates: copper, aluminum, and brass for various substrate temperatures, ranging from $0^\circ C$ to $-15^\circ C$. The corresponding Stefan number (Ste)

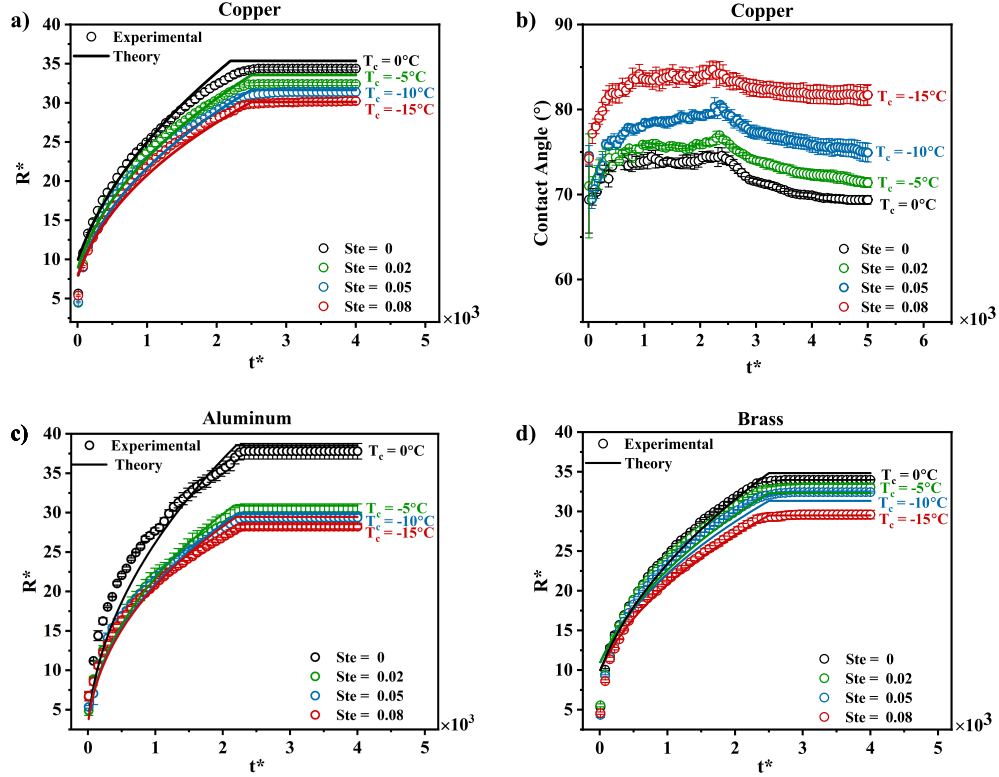


Figure 2.3: Compares the experimental observations for non dimensional drop spreading radius R^* of a $6\mu l$, with the predicted theoretical results for different Stefan number, Ste , which is achieved by varying substrate temperatures (T_c) (a) for copper substrate. (b) corresponding contact angle measurements. (c) for aluminum substrate (d) for brass substrate

is given as $\frac{C_p \Delta T}{L_f}$ which is a function of $\Delta T = T_m - T_c$ (T_m is the melting temperature and T_c is the substrate temperature).

Fig. 2.3 (a) represents the dynamics of droplet growth on a copper substrate, where the drop was generated by mass addition through a liquid jet. During the drop generation on a solid substrate via the liquid jet, the drop radius increases with time, which can also be observed from the monotonous growth or spreading of the non-dimensional radius R^* with respect to non-dimensional time, t^* in Fig. 2.3(a). The spreading of the drop ceases to progress once the jet is stopped. Further analysis of Fig. 2.3(a) reveals that the spreading rate on a substrate at subzero temperature

is slower than on the substrate at $0^\circ C$. From Fig. 2.3(a), the slope at $T_c = 0^\circ C$ is 8.67×10^{-3} and the slope at $T_c = -15^\circ C$ is 7.42×10^{-3} . From this observation, it is evident that the spreading rate ($\frac{dR^*}{dt^*}$) is getting slower with increasing Ste , aligning with the existing literature [16, 42]. Along with the slower spreading rate, we can also observe that the final radius of the drop has an inverse proportional relationship to Ste . The reason behind this inversely proportional relationship can be attributed to additional energy dissipation toward the energy gradient as a result of the higher temperature difference between the liquid phase and solid substrate. A detailed analysis of nondimensional numbers on the spreading ratio has been explained in the Appendix. A.

It is worth mentioning that for $Ste > 0.08$, the drop ceases to spread earlier due to TPCL arrest, as shown in Fig. 2.4 (a). When the temperature of the substrate is low enough (less than $-15^\circ C$), the drop freezes as soon as it is in contact with the substrate and only grows toward the direction in which mass is being added without changing its base radius, as shown in Fig. 2.4 (a). The thermal properties of the liquid and solid substrates play an important role in the arrest of the contact line. At $Ste > 0.08$, when the jet lands on the cold metal substrate with higher thermal conductivity, nucleation begins immediately and ice crystal formation and radial growth of ice crystals along with the substrate occur, as observed by Grivet et al. [16]. Therefore, at lower temperature, the radial velocity of the ice crystal growth quickly catches up and subsequently overcomes the spreading velocity of the drop, and as a result, the TPCL gets arrested and stops moving. However, this crystal growth at lower temperatures is highly probabilistic in nature [68]. This results in frequent occurrence of stick-slip behavior, which is why it is regarded as non-reproducible. Therefore, it is the main reason for us to refrain from comparing the theoretical model with the experimental analysis when $Ste > 0.08$

	0°C	-5° C	-10° C	-15° C
Copper	73.7 ± 0.9°	75.2 ± 0.3°	77.8 ± 0.6°	82.8 ± 1.1°
Aluminum	38.7 ± 6.4°	54.8 ± 4.9°	55.5 ± 2.9°	62.7 ± 0.9°
Brass	80.8 ± 1.7°	83.1 ± 1.1°	83.3 ± 1.5°	85.8 ± 1.2°

Table 2.2: The dynamic contact angle during the propagation of TPCL until it reaches equilibrium

Fig. 2.3 (b) shows the evolution of the dynamic contact angle for a droplet $6\mu l$ on a copper substrate for varying Ste . The variation in contact angle with respect to temperature has already been reported elsewhere[80, 81]. However, the temperature range that has been analyzed by previous studies ranged from $5^{\circ}C - 130^{\circ}C$ to [81], and from these studies it has been observed that the contact angle increased with a decrease in temperature. However, in the present study, we measured the contact angle at a subzero temperature. We observed that the contact angle increases as the substrate temperature decreases, which is consistent with previous studies. A similar contact angle - temperature relationship can also be observed for other substrates that are used for this study, such as aluminum and brass. The inverse relationship between contact angle and substrate temperature can be clearly seen in Table 2.2. The change in the surface tension (liquid-air interface) of the liquid once the liquid touches the substrate can be one of the major causes for the variation in the contact angle. From the literature, the surface free energy (SFE) value at room temperature ($T_C = 20^{\circ}C$) for bare flame treated copper was found to be $\approx 60mN/m$ [45] and we performed a similar experiment for substrate temperature at $-5^{\circ}C$ and observed an SFE value of $\approx 50mN/m$, respectively. The SFE of the flamed copper is found to decrease with temperature. However, this analysis of the temperature dependence of SFE is not in the scope of this study, and that is why we will refrain from further analysis of this topic.

Similarly to copper, the experimental curves for aluminum and brass substrates shown in Figs.2.3 (c) and (d) illustrate the increasing trend of the spreading rate (R^*) over time (t^*), followed by a plateau. However, a sudden drop in the spreading rate can be observed from $Ste = 0$ to $Ste = 0.03$ for aluminum substrates. This could be due to the rapid development of a thin oxide layer that can affect the surface properties of aluminum [82]. Despite the use of flame treatment to address this concern, its effectiveness may vary due to human involvement. Although contact angle measurements for aluminum may be erroneous (as shown in the Table. 2.2), due to the assumption of a constant dynamic contact angle and utilizing experimental data to solve the governing equation. 2.9, the theoretical model is still able to predict the spreading rate on an aluminum surface. From Figs. 2.3 (a), (c) and (d), it is evident that the theoretical predictions closely ($\pm 5\%$) match the experimental observations, confirming the validity of the model with different operating conditions. The effect of Ste on the spreading rate is consistent with the observations in copper, where lower temperatures tend to slows the spreading, resulting in smaller (R^*). Across all substrates, the variations of the Stefan number indicate the influence of latent heat during the phase-change process. Lower Ste numbers correspond to slower heat transfer rates, reflecting a slower freezing process, which can be observed through the reduced gradient in the initial spreading phase for both experimental and theoretical curves.

2.4.5 Freezing dynamics

In order to analyze the freezing dynamics of the spreading droplet we have to again revisit the Fig. 2.2, which depicts the different stages associated with the whole freezing process. As depicted in Fig. 2.2, the freezing process starts with *Stage – IV* nucleation / recalescence and ends with tip formation at *Stage – VI*. It is to be noted that extensive research has been conducted on *Stage – VI*, where the important takeaway is the universal behavior in the tip cone angle, which occurs due to

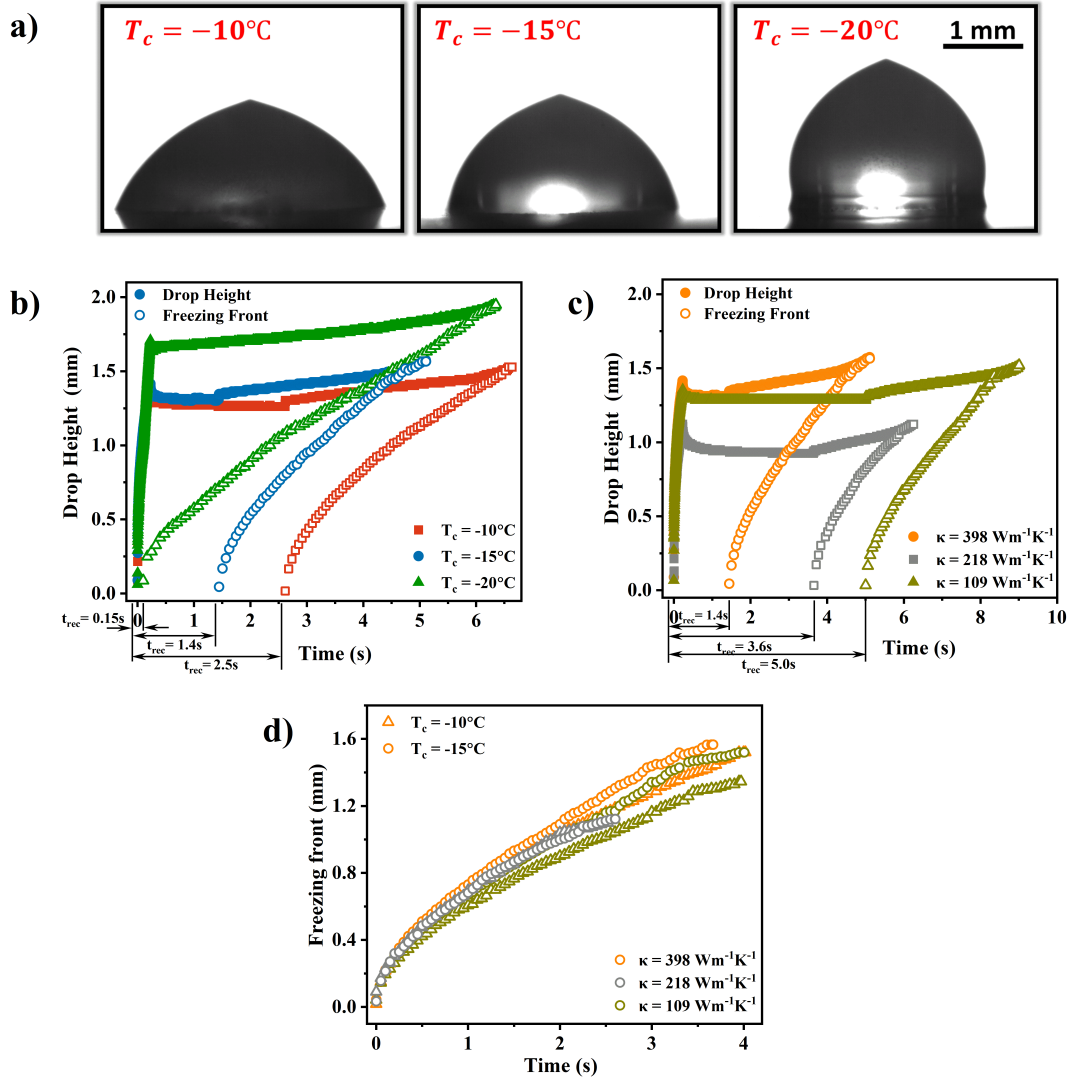


Figure 2.4: (a) The final shape formed by frozen droplet on copper substrate maintained at -10°C , -15°C & -20°C . The droplet height and corresponding freezing front of droplet during the entire spreading and freezing process for (b) copper substrate maintained at temperatures -10 , -15 , -20°C . (c) copper, aluminum and brass maintained at fixed surface temperature of -15°C . (d) freezing front of $6\mu\text{l}$ droplet on copper, aluminum and brass maintained at -10 , -15°C . The start of freezing is set as the beginning of the freezing front.

the liquid-solid density ratio [53, 54, 73]. Therefore, the main emphasis of this study is on *Stage – IV* & *V*, where we critically investigate the initiation of the freezing process. Here, the time delay for the initiation of the freezing process is denoted by t_{rec} , which can be defined as the duration from the moment the jet strikes to the onset of *Stage – IV*, that is, the recalescence stage. .

Fig. 2.4 (a) is the experimental observations of the final shape of the frozen droplet on the copper substrate maintained at $-10^{\circ}C$, $-15^{\circ}C$ & $-20^{\circ}C$. For an effective representation of the time delay t_{rec} , the propagation of the drop height with the freezing front has been plotted and represented in Fig. 2.4 (b) for various temperatures of the copper substrate. For a fixed volume and on a given substrate (copper), as shown in Fig. 2.4 (b), when the surface temperature varies $-10^{\circ}C$, $-15^{\circ}C$ & $-20^{\circ}C$, it becomes evident that as the temperature decreases, the time delay also decreases from 2.5s to 0.15s. It can be seen that there is a delay in the commencement of the freezing process. For $T_c = -10^{\circ}C$ & $-15^{\circ}C$, freezing begins 2.5s & 1.4s, respectively, after jet impact, which indicates that the lower the temperature, the shorter the time delay. An extremely shorter time delay has been observed for $T_c = -20^{\circ}C$, where the freezing process started immediately after the jet strikes the substrate. Due to this scenario, we could not see the recalescence stage and therefore t_{rec} is very small for this scenario.

In case of the lowest surface temperature $T_c = -20^{\circ}C$ we observed two contradictory observations: i) the time at which the freezing starts (t_{rec}) which is the shortest, but (ii) the total freezing time to form the tip cone, which is the longest for this scenario. At $T_c = -10^{\circ}C$ & $-15^{\circ}C$, the total freezing time is almost similar ($\approx 3.5s$), while at $T_c = -20^{\circ}C$ it is significantly higher $\approx 6s$. At this $T_c = -20^{\circ}C$, the radial growth of the ice crystal occurs at the jet-substrate interface [16, 42] at time, $t = 0s$, and due to the extreme low temperature, the radial velocity of the ice crystal exceeds

the velocity of the spreading drop as quickly as $t = 0.15s$. As a result, the TPCL was pinned, while the drop is still forming along its height with the addition of mass from the jet, as shown in Fig. 2.4 (a). Due to the pinned TPCL, at $T_c = -20^\circ C$ we can observe a larger solidified drop height ($\approx 2mm$), compared to $T_c = -10^\circ C$ & $-15^\circ C$ where the solidified drop height is almost identical ($\approx 1.5mm$). At $T_c = -20^\circ C$, due to the lower drop-substrate contact area and the higher height, the freezing front has to travel a longer distance to complete the freezing process. Therefore, even though the substrate temperature is lower ($-20^\circ C$), we can observe slower freezing dynamics after jet deposition.

Similarly, for a fixed droplet volume and substrate temperature of $6\mu l$ & $T_c = -15^\circ C$ respectively and varying the thermal conductivity, as shown in Fig. 2.4 (b), it is observed that with increasing thermal conductivity, both t_{rec} and the total freezing time decrease. The difference in t_{rec} between these materials suggests that thermal conductivity plays a crucial role in the time required for nucleation to occur. Copper, known for its high thermal conductivity, shows the fastest $t_{rec} = 1.4s$, indicating a faster nucleation rate. On the contrary, brass and aluminum, with lower thermal conductivity, exhibit delayed nucleation, which is reflected in longer $t_{rec} = 3.6s$ & $5s$ respectively. Despite the fact that surface properties and temperature play a crucial role in nucleation/recalcescence, as well as the total freezing time, the rate of propagation of the freezing front is independent of the thermal properties of the drop and the substrate. This can be seen by offsetting the time delay and resetting the time to zero at the start of a freezing front, as shown in Fig. 2.4 (c). The experimental results of the freezing rate on copper, aluminum, and brass substrates at $-10^\circ C$ & $-15^\circ C$ are plotted in Fig. 2.4 (c). It is observed that there is initially a very minimal difference in the freezing rate, and it decreases as the surface temperature decreases. This is due to the low thermal conductivity of the ice layer that is formed.

2.5 Conclusion

Our study investigated the simultaneous spreading and freezing of sessile droplets, particularly using a jet-based dosing technique.

- Shadowgraphic and thermal imaging was used to elucidate the distinct stages involved in jet-based approach. From the thermal profiles we observed the absence of supercooling effect where the drop is deposited using a jet. This is because of the competition between heat transfer and mass addition.
- We employ a comprehensive theoretical model based on the Overall Energy Balance (OEB) approach to determine the transient spreading of TPCL considering heat transfer from the impinging cold substrate. Appropriate length, time, and temperature scales were used to non-dimensionalize the governing equations. Experimental findings were used to validate the theoretical prediction, and we observed a reasonable agreement of $\pm 5\%$. A decreasing trend in the spreading rate and an increase in the contact angle are observed as Ste increases. This signifies the influence of solidification on damping of the movement of the TPCL.
- With a further increase in $Ste > 0.08$, we observed that TPCL is arrested as the mass is still added. This is because the velocity of the ice layer is greater than the TPCL velocity. For $Ste > 0.08$, we observed that nucleation / recalescence occurred faster, but the total freezing time was slower. This is due to an increase in the droplet height, which causes the freezing front to travel longer. When the thermal conductivity of the substrate is decreased, the nucleation / recalescence time (t_{rec}) increases, resulting in a longer freezing time. Although the surface parameters influence the nucleation/ recalescence time, there is minimal difference in the freezing front rate.

Chapter 3

Universality of Frozen Water Droplet

3.1 Abstract

The universal behavior of the angle caused by the so-called "pointy tip" of a frozen droplet is widely accepted. Is this behavior of the tip angle universally applicable regardless of the shape of the drop? For a better perspective of this, we observed that, for a given density ratio, the ratio between the height of solidified drop and the liquid drop is constant, irrespective of the droplet's shape. This can be considered as the true universality of the frozen droplet. This is true for a wide range of experimental conditions that might affect the form of the droplet. First, we observed the case of symmetric and asymmetric shaped droplets. Then we froze the drop in parabolic flight that simulates micro-gravity, martian-gravity, and hyper-gravity. This wide spectrum of experiments necessitated a more general theoretical model that can predict the frozen droplet height and, in turn, the solid-liquid height ratio. The "two-triangle" approach used in the present study was able to predict the solid drop height with reasonable agreement compared to existing approaches. We observed the universal behavior of the solid-liquid height ratio for all of the experimental conditions.

3.2 Introduction

When liquids undergo the process of solidification, intricate and multifaceted phenomena ensue. A focal point of investigation within this domain pertains to the solidification of water droplets, motivated by the urgent need for a better understanding of the freezing dynamics attributed to its widespread applications and the safety implications associated with the accretion of ice [71]. As a consequence, there has been a discernible increase in research efforts aimed at elucidating the mechanisms that govern the freezing of liquids and the subsequent solidification of droplets [51, 71, 76, 83]. Multiple investigations corroborate that the disparity in density between the solid and liquid phases, exemplified by water and ice, induces a volumetric alteration, causing the freezing ice front to protrude beyond the liquid-gas interface. This phenomenon engenders the formation of a distinctive structure colloquially denominated as a “pointy ice drop” [49, 50]. Despite the inherent tendency of surface tension to deter the emergence of pointed features, the density incongruity between the liquid and solid phases instigates the manifestation of a cusped singularity [8, 49].

The universal behavior of the tip-cone angle persists in various freezing conditions, as initially observed for symmetric droplets under different contact angles and surface temperatures [53]. This universality extends to asymmetric droplet freezing, which is more prevalent in practical applications than symmetric freezing [54], and even when droplets freeze upside down [8]. In the context of droplet freezing, the release of latent heat during front propagation significantly influences the final droplet shape. This effect arises from the improved heat transfer to the cold substrate compared to the heat released into the surrounding ambient air [46]. Furthermore, the frozen droplet’s shape can be modulated by adjusting the heat flux at the solid base, even in the case of asymmetric droplets, where the direction of the heat flux influences the position of

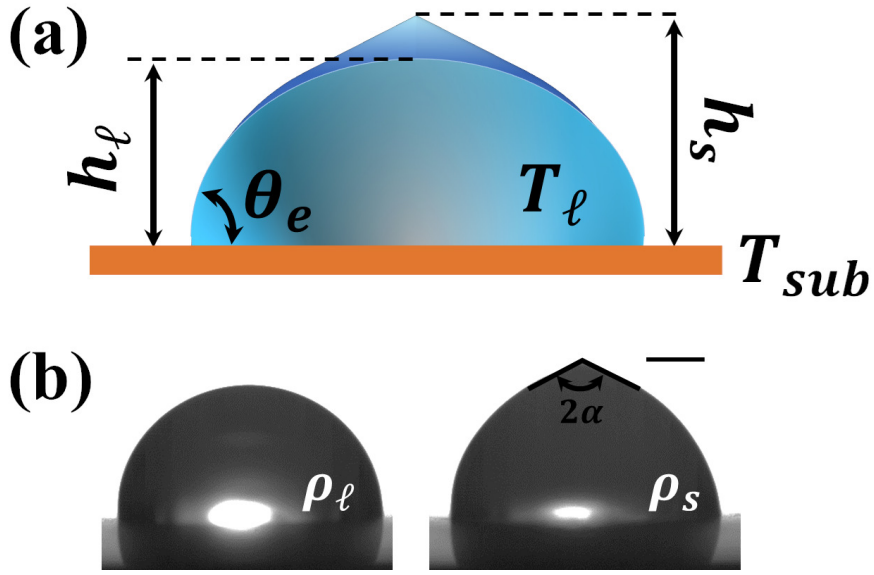


Figure 3.1: (a) Schematic diagram of water drop before and after freezing. h_s & h_l represent the heights of solid and liquid drop heights respectively. θ_e is the contact angle made by the drop which initially maintained at temperature T_ℓ and dosed on a substrate at temperature T_{sub} (b) Experimental snapshots of liquid and solid water droplet with corresponding densities. Also shows the tip cone angle 2α . Scale bar represents $1mm$.

the tip while maintaining the universal behavior of the tip angle [8].

The following inquiry arises: Can the universality observed at the tip-cone angle be deemed genuine universality? The succinct response is negative, as it neglects consideration of the droplet's shape. In an effort to rectify this limitation and attain a more comprehensive understanding of authentic universal behavior in frozen droplets, this letter presents evidence that, for a given liquid-to-solid density ratio, the ratio between the solid drop height (h_s) and the liquid drop height (h_l) remains constant regardless of the freezing parameters. This constancy is confirmed for both symmetric and asymmetric droplets. Furthermore, our investigation expands to encompass observations under gravitational forces that can affect droplet morphology. Beyond establishing universality in the height ratio, our study asserts that the two-triangle approach surpasses alternative methods, such as the average contact angle method

and the heat transfer model, in accurately predicting the height ratio.

3.3 Experimental description

In this investigation, we conducted a comprehensive series of experiments to explore the freezing of droplets deposited on various metal substrates on Earth and microgravity. The droplets were carefully observed and analyzed from a side-view, as illustrated in Fig. 3.1 (b). We deposited water droplets in different volumes ($3 - 20\mu L$) on four metal substrates (aluminum, brass, copper, and titanium). In this study, we used deionized water, which was degasified by removing dissolved gases using a vacuum pump. To ensure precise control over experimental conditions, all tests were carried out within a carefully regulated liquid-cooled temperature controlled environment (TC40, Krüss), maintaining temperatures between -5° and $-15^\circ C$. After droplet deposition, we induced asymmetry by tilting the substrate at specific angles within the range of $0 - 90$ deg. The larger and smaller contact angles of the droplets are termed the advancing and receding contact angles, respectively. In a typical contact angle hysteresis study, the advancing and receding angles are usually defined on the onset droplet sliding on the tilted substrate. However, in this study, to articulate the drop shape asymmetry, we strictly avoided sliding of the droplets; therefore, the advancing and receding contact angles defined in this study do not represent contact angle hysteresis.

Moreover, we conducted reduced gravity experiments by enclosing the entire experimental setup within a pelican case ($47.5cm \times 47.5cm \times 47.5cm$). This set-up was subsequently installed in a parabolic flight that simulated microgravity, martian gravity, and hypergravity. The parabolic flight facility, provided by the Flight Research Laboratory in Ottawa, Canada, enabled the desired gravitational fields to be observed for $20 - 23$ seconds. All experiments performed with parabolic flights are for

symmetric drops since tilting the substrate during parabolic maneuvers was an engineering challenge. A detailed description of parabolic flight maneuvers with relevant acceleration profiles and experimental setup can be found in our previous studies [45].

3.4 Theroretical Model

3.4.1 Tip angle vs density ratio

The relation between the density ratio ν and the tip cone angle α can be determined by measuring volumes during the final stages of freezing, as shown in Fig. 3.2. This was discussed in detail in the work of Schetnikov et al. [50]. The volumes obtained during the final stages of droplet freezing are divided into three parts, that is, V_1 and V_2 are the volumes of the unfrozen drop and V_c is the volume after the drop is frozen, as shown in Fig. 3.2. The following equations determine the corresponding volumes during each stage[50].

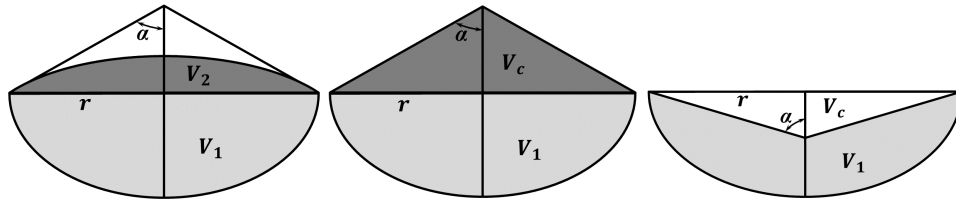


Figure 3.2: Volumes during the final stages of the drop freezing for unfrozen drop, tip formation and dimple formation

$$V_1(\alpha) = \frac{\pi r^3}{3} \frac{(1 - \cos \alpha)^2 (2 + \cos \alpha)}{\sin^3 \alpha} \quad (3.1)$$

$$V_2(\alpha) = \frac{\pi r^3}{3} \frac{(1 - \sin \alpha)^2 (2 + \sin \alpha)}{\cos^3 \alpha} \quad (3.2)$$

$$V_c(\alpha) = \frac{\pi r^3}{3} \frac{\cos \alpha}{\sin \alpha} \quad (3.3)$$

The difference in the sum of the volumes is equated with the density ratio to determine the corresponding tip-cone angle.

$$\nu = \frac{V_1(\alpha) + V_2(\alpha)}{V_1(\alpha) + V_c(\alpha)} \quad (3.4)$$

When ν is greater than one, the formation of a dimple-like curvature can be observed. This is determined by removing the final volume V_c from V_1 as shown in Fig. 3.2.

$$\nu = \frac{V_1(\alpha) + V_2(\alpha)}{V_1(\alpha) - V_c(\alpha)} \quad (3.5)$$

3.4.2 Two Triangle Approach

To the best of our knowledge, studies on measuring and predicting the frozen drop height for asymmetric case are limited. For simplicity purposes, the average contact angle θ_{av} is used [84]. This approach is erroneous; therefore, the two-circle method was proposed by ElSherbini et al. [85]. However, both approaches are restricted only to liquid droplet heights. Therefore, in this study, the two-triangle method was proposed that can overcome these limitations. For a symmetric drop, with circular TPCL, the drop shape is generally characterized by an equilibrium contact angle θ_e with minimal contact angle hysteresis. Commonly, this drop shape appears to be a symmetric drop in goniometric measurements. On the other hand, the two-triangle method employs the advancing contact angle, denoted as θ_A , and the receding contact angle, denoted as θ_R , of the asymmetric frozen droplet to generate two symmetric droplets that overlap one another. Two isosceles triangles, as shown in Fig. 3.3 (d) are constructed using the symmetric drops with the assumption of $\alpha_A = \alpha_R = \alpha$ based on the experimental observation. Heights h_A and h_R , corresponding to the advancing and receding contact angles, respectively. By superimposing these two isosceles triangles, we can determine the original height of the frozen asymmetric droplet h_s .

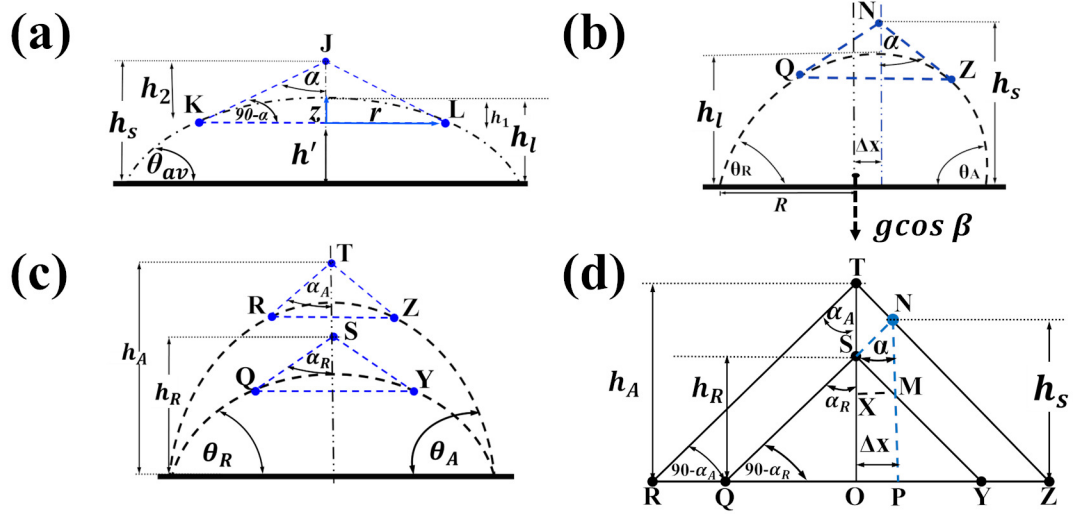


Figure 3.3: (a) Parameters involved in theoretical modeling for symmetric drop having an initial contact angle θ_{av} ; h_i and h_w are the maximum height of the droplet in the solid and liquid phases, respectively; r and z are the radius and height of the solid-liquid interface at any time, respectively; h' is the height of the frozen part at any time, h_1 is the unfrozen part at that time, and h_2 is the final frozen part of the remaining height h_1 of the droplet. (b) Asymmetric drop having different initial contact angles, that is, the advancing contact angle θ_A and the receding contact angle θ_R with universal tip angle α . (c) Two superimposed symmetric droplets having initial contact angles of the asymmetric drop, that is, θ_A and θ_R ($\theta_A > \theta_R$). Based on these two different contact angles, we find two different corresponding heights of h_A and h_R , respectively, but due to the universality of the tip angle of drop freezing, we observe $\alpha_A = \alpha_R = \alpha$. (d) The theoretical basis of the two-triangle approach to predict asymmetric drop parameters: the approach indicates that $h_A < h_i < h_R$ with the assumption of $\alpha_A = \alpha_R = \alpha$ based on experimental observation.

The contour of a solidified drop can be determined by the evolution of the liquid volume and the solid-liquid interface [51]. The differential equations that govern the shape of the frozen droplet are given by [49, 53, 54].

$$\begin{aligned} \frac{d}{dh}(V_l + \nu V_s) &= 0, \\ \frac{dh}{dR} &= -\tan \theta, \end{aligned} \quad (3.6)$$

The height of the symmetric drops generated by the advancing and receding contact angles (h_A & h_R) can be determined by solving the above equations, where $V_{l,s}$ are the volumes of the liquid and solid portions. $\triangle TRZ$ and $\triangle SQY$ in Fig. 3.3(c) are

the two superimposed isosceles triangles based on the advancing and receding contact angle, respectively. From Fig. 3.3 (d), we can write the following:

$$\begin{aligned}
OT &= h_A \\
OS &= h_R \\
OQ &= OS \tan \alpha_R = h_R \tan \alpha \\
OR &= OT \tan \alpha_A = h_A \tan \alpha \\
MN &= ST = OT - OS = h_A - h_R \\
\angle MSN &= 180^\circ - 2\alpha = \beta
\end{aligned} \tag{3.7}$$

Now applying the sine rule for the $\triangle MSN$ we can establish the following relationship:

$$\begin{aligned}
\frac{MN}{\sin \beta} &= \frac{SM}{\sin \alpha} \\
\therefore SM &= MN \frac{\sin \alpha}{\sin \beta}
\end{aligned} \tag{3.8}$$

Now considering equations 3.7 and 3.8 we can write the following expression,

$$SM = (h_A - h_R) \frac{\sin \alpha}{\sin 2\alpha} = \frac{h_A - h_R}{2 \cos \alpha} \tag{3.9}$$

Taking into account eq. 3.8 and $\triangle SMX$, the expression for tip shifting, $OP = MX = \Delta X$ can be determined by the following equation,

$$\begin{aligned}
MX &= SM \sin \alpha = \frac{h_A - h_R}{2 \cos \alpha} \sin \alpha \\
\therefore \Delta X &= \frac{h_A - h_R}{2} \tan \alpha
\end{aligned} \tag{3.10}$$

From $\triangle OSY$, $OY = OS \tan \alpha = h_R \tan \alpha$ and $PY = OY - OP = h_R \tan \alpha - \frac{h_A - h_R}{2} \tan \alpha$. Now taking into account the expression for OY and PY , we can write the following expression for PM ,

$$\begin{aligned}
PM &= PY \tan(90 - \alpha) \\
&= \left[h_R \tan \alpha - \frac{h_A - h_R}{2} \tan \alpha \right] \cot \alpha \\
&= \left[h_R \tan \alpha - \frac{h_A - h_R}{2} \tan \alpha \right] \frac{1}{\tan \alpha} \\
\therefore PM &= \frac{3}{2} h_R - \frac{1}{2} h_A
\end{aligned} \tag{3.11}$$

Finally, considering Eq. 3.11 we can derive the height h_s of the frozen droplet from the following equation,

$$\begin{aligned}
h_s &= PN = MN + PM = (h_A - h_R) + \frac{3}{2}h_R - \frac{1}{2}h_A \\
\therefore h_s &= \frac{h_A + h_R}{2}
\end{aligned} \tag{3.12}$$

3.4.3 Heat Transfer Model

The heat transfer model considers one-dimensional heat conduction at the solid-liquid interface [10, 51]. Mass conservation at the interface of the freezing front gives the relation between the unfrozen liquid and ice, given by [10, 70, 74]:

$$\frac{dV}{dt} = -\pi\nu R^2 \frac{dh}{dt} \tag{3.13}$$

Where V is the volume of the drop, ν is the density ratio (for water $\nu = 0.917$), h is the thickness of the freezing front, and R is the base radius of the drop. Taking into account the one-dimensional Stefan problem and the quasi-steady state approximation, the energy balance equation at the ice-water interface yields [10, 70, 74]:

$$q_s - q_l = \rho_i L_f \frac{dh}{dt} \tag{3.14}$$

Here $q_{s,l}$ are the heat fluxes for the ice and liquid phases and L is the latent heat transfer of water. At the freezing point, the q_l is zero, and we assume that the freezing from the process is quasi-steady and linear temperature distribution Eq. 3.14 can be written as

$$\frac{k_i \Delta T}{h} = \rho_i L_f \frac{dh}{dt} \quad (3.15)$$

where k_i is the thermal conductivity of the ice. $\Delta T = T_m - T_c$ where T_m is the melting/freezing temperature and T_c is the surface temperature. After integrating Eq. 3.15 we get the final governing equation for the freezing front [10, 51, 70, 74].

$$h_s = z = \sqrt{\frac{2k_i \Delta T}{\rho_i L_f} t} \quad (3.16)$$

where, the solid thermal conductivity (k), the solid density (ρ_s), the latent heat of the fusion (L_f), the difference in temperature (ΔT) are physical properties.

3.4.4 Average contact angle approach

Although the average contact angle (ACA) or symmetric drop approach was originally devised to predict the behavior of asymmetric liquid drops on the verge of sliding [84], our present investigation extends its application to predict the ratio of the height of the solid drop to the height of the liquid drop in the context of asymmetric frozen drops. The relevant parameters involved in the theoretical modeling of the average contact angle approach include the initial contact angle θ_{av} , where $\theta_{av} = (\theta_A + \theta_R)/2$. The maximum heights of the droplets in the solid and liquid phases are denoted as h_s and h_ℓ , respectively. The average contact angle theory simplifies the drop shape problem by considering a spherical cap approximation. This leads to the assumption of a constant contact angle throughout the circumference of the drop. Therefore, a contact angle θ_{avg} , which is the average of the advancing and receding contact angles, is used to determine the volume of the drop [85]. Let V be the volume of any corresponding height h . Therefore, from Fig. 3.3 (a) we can derive the expression of the ice-to-water drop volume ratio as follows [50]:

$$\frac{V(h_w)}{V(h_i)} = \frac{V(h_w)}{V(h_w) - V(h_1) + V(h_2)} = \nu = 0.92 \quad (3.17)$$

where $V(h_1)$ and $V(h_2)$ are the volumes of unfrozen liquid and frozen ice in the final stages of freezing [50]. These are determined as follows.

The base for $V(h_1)$ and $V(h_2)$ can be obtained by

$$r = h_2 \tan \alpha \quad (3.18)$$

Again we can write for unfrozen drop volume $V(h_1)$

$$r = h_1 \cot \frac{90 - \alpha}{2} \quad (3.19)$$

Therefore, the spherical cap and cone equations are used to determine volumes $V(h_1)$ and $V(h_2)$, respectively.

$$\begin{aligned} V(h_2) &= \frac{\pi}{3} r^3 \cot \alpha = \frac{\pi}{3} (4.6) h_1^3 \\ V(h_1) &= \frac{\pi}{3} r^3 \frac{2 - 3 \sin \alpha + \sin^3 \alpha}{\cos^3 \alpha} \end{aligned} \quad (3.20)$$

So, the volume ratio between the unfrozen and the frozen volumes in the final stage of freezing is given by

$$\frac{V(h_1)}{V(h_2)} = 0.92 \Rightarrow h_1 = 0.476 h_2 \quad (3.21)$$

Now, if R is the initial droplet radius and θ_{av} is the droplet average contact angle, then

$$f(\theta_{av}) = \frac{2 - 3 \cos \theta_{av} + \cos^3 \theta_{av}}{\sin^3 \theta_{av}} \quad (3.22)$$

And

$$f(\alpha) = \frac{2 - 3 \sin \alpha + \sin^3 \alpha}{\cos^3 \alpha} \quad (3.23)$$

Thus, the volume of the total unfrozen liquid is given by

$$V(h_w) = \frac{\pi}{3} R^3 f(\theta_{av}) \quad (3.24)$$

Plug in all the values in Eq.3.17.

$$\frac{V(h_w)}{V(h_i)} = \frac{\frac{\pi}{3}R^3 f(\theta_{av})}{(\frac{\pi}{3}R^3 f(\theta_{av})) - (\frac{\pi}{3}r^3 f(\alpha) + (\frac{\pi}{3}r^3 \cot\alpha))} = \nu = 0.92 \quad (3.25)$$

$$\left(\frac{1}{\nu} - 1\right)f(\theta_{av})(R)^3 = (\tan \alpha)^2 h_2^3 - h_2^3 (\tan \alpha)^3 f(\alpha) \quad (3.26)$$

Taking $\alpha = 65^\circ$, we get:

$$0.0099(f(\theta_{av}))R^3 = -31h_1^3 = 1.26h_2^3 \quad (3.27)$$

Thus, taking 3.18, $\tan \frac{\theta_{ac}}{2} = \frac{h_w}{R}$

From Eq.3.27 we get

$$\frac{h_w}{h_2} = \frac{2.335 \tan \frac{\theta_{av}}{2}}{f(\theta_{av})^{\frac{1}{3}}} \quad (3.28)$$

Now,

$$h' = h_w - h_1 = h_i - h_2 \quad (3.29)$$

Thus,

$$h_w = h_i - 0.524h_2 \Rightarrow h_i = h_w + 0.24 \frac{h_w f(\theta_{av})^{\frac{1}{3}}}{\tan \frac{\theta_{av}}{2}} \quad (3.30)$$

We can rewrite the general form as follows:

$$\frac{h_s}{h_\ell} = 1 + \left[\sqrt[3]{\frac{\frac{1}{\nu} - 1}{(\tan \alpha)^2 - f(\alpha)(\tan \alpha)^3}} \right] \frac{f(\theta_{av})^{\frac{1}{3}}}{\tan \frac{\theta_{av}}{2}} \quad (3.31)$$

Thus, the equation 3.31 is the representation of the height ratio of ice and water, indicating that $h_s/h_\ell \geq 1$ for all cases as long as $\nu \leq 1$. It is worth noting that the average contact angle may still be inaccurate, since it is developed primarily for the liquid drop height, and as a consequence it may predict the additional height due to the protrusion of the pointy shape of the solidified drop with a larger error margin.

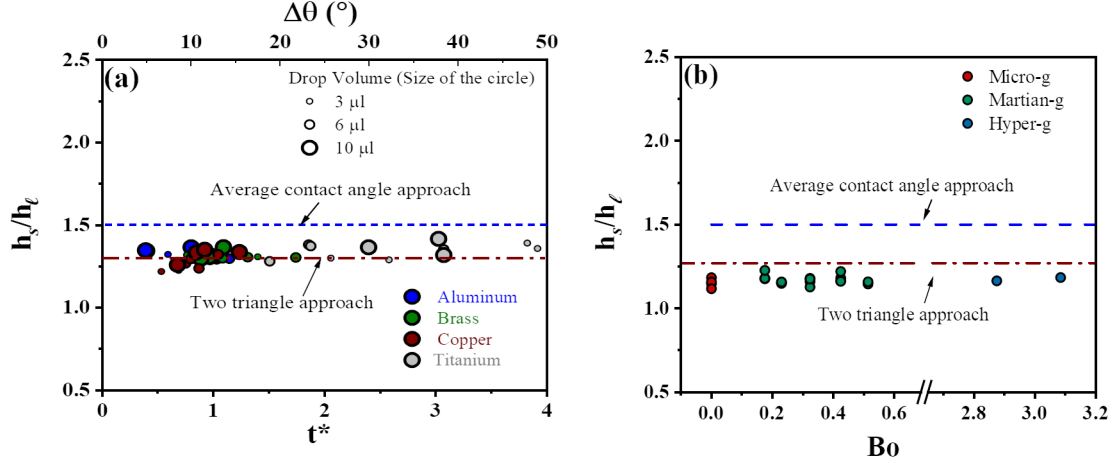


Figure 3.4: (a) Ice h_s to water h_ℓ height ratio for symmetric and asymmetric drop. For the difference in contact angle $\leq 50^\circ$, this height ratio varies within 1.2 and 1.6. Within our experimental range, the two triangle approach suggests the height ratio of 1.27 while the new average contact angle approach suggests 1.5. (b) Ice h_s to water h_ℓ height ratio for symmetric and asymmetric drop as a function of gravitational field which can be represented by a non-dimensional Bond number.

3.5 Results and discussion

For the operating conditions (substrate thermal conductivity ranging from 20 to 400 $Wm^{-1}K^{-1}$, temperature up to $-15^\circ C$ and water drop) that we have used, we can observe universality in the ratio of frozen drop height (h_s) to the liquid drop height (h_ℓ), i.e., h_s/h_ℓ . Regardless of substrate properties and freezing rate, the experimentally observed h_s/h_ℓ is 1.25 ± 0.04 as shown in Fig. 3.4 (a). From this observation it is evident that for a certain density ratio the solid-to-liquid height ratio always remains the same. h_s/h_ℓ calculated from the two-triangle approach is ~ 1.27 , while h_s/h_ℓ is ~ 1.5 when calculated from the average contact angle approach. From this analysis we can argue that, though both the two-triangle and average contact angle approaches can predict the freezing drop height closer to the observed height, the two-triangle approach is better at predicting the frozen drop height.

In Fig. 3.4 (b), it is evident that the ratio h_s/h_ℓ remains independent of the strength

of the body forces. To achieve these results, we conducted experiments under various gravitational conditions, including microgravity, Martian gravity, terrestrial gravity, and hypergravity. For the gravitational body-force scenario, we used deionized water. To demonstrate the interplay between surface forces and body forces, we presented the height ratio as a function of the effective Bond number $Bo = \frac{\rho g D^2}{\sigma_{lv}}$ [86], where D is the diameter of a spherical drop, which is also the characteristic length, g is the acceleration due to gravity.

Fig. 3.4(b) indicates that h_s/h_ℓ remains constant regardless of the strength of gravity. It is noteworthy to mention that, due to time constraints during the parabolic flight experiments, we deposited the droplet on an already cooled copper substrate at a subzero temperature. Under this condition, we observed $h_s/h_\ell \sim 1.2$. On the contrary, in terrestrial gravity, when we deposited the drop on a substrate at room temperature and then started the freezing process, we observed a slightly different value of $h_s/h_\ell \sim 1.25$. Regardless of the specific operating conditions, it is evident from the results that the two-triangle approach effectively predicts the magnitude of h_s/h_ℓ .

It is well understood and documented that the tip angle, of the frozen drop is a function of the density ratio of the liquid and solid phases, regardless of the shape of the drop shape [50]. Unlike the tip angle, the height of the frozen drop requires information on the shape of the drop [51], which is dictated primarily by the contact angle. Irrespective of the shape of the TPCL or the asymmetry in the drop shape, the heat-transfer model is proposed. The primary assumption of the heat transfer model is one-dimensional transport leading to a one-dimensional progression of the solid-liquid interface [51]. Another assumption of a flat solid-liquid interface in droplet freezing simplifies the prediction of interface movement by neglecting the complexities of interface curvature, enabling more straightforward analysis of phase transition

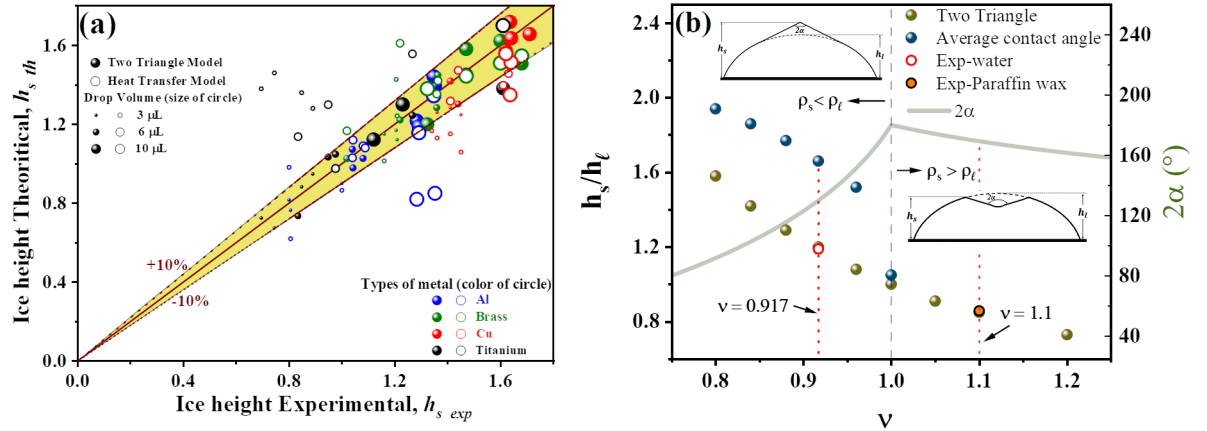


Figure 3.5: (a) Asymmetric drop maximum height (h_s) prediction: We compare the two-triangle approach and the heat transfer model with our experimental results. Filled and empty circles represent the two triangle and heat transfer approaches, respectively. We investigate asymmetric drop freezing with four different metals for three different drop volumes. (b) Solid-liquid height ratio for different density ratios predicted by the two-triangle and average contact angle approach. The green line indicates the Tip cone angle for corresponding density ratios. The blue dashed line separates the plot at $\nu = 1$ representing the symmetric drop limitation. The images inscribed in the plot show the tip formation when $\nu < 1$ and the dimple formation when $\nu > 1$. The red dotted line highlights the height ratios predicted by both theoretical and experimental results and the respective tip angle for the case of water and paraffin wax

dynamics. During the propagation of the ice layer, a quasi-steady-state assumption leads to equating the heat released by the solid phase to the latent heat released from the liquid phase. The instantaneous location of the moving solid-liquid interface is given by Eq. 3.16

The height of the frozen droplet is established based on the final freezing time, which can be derived by numerical calculations [7] or obtained through experimental measurements [87]. Consequently, employing a heat transfer model to predict the frozen droplet's height becomes a complex task because it necessitates knowledge of the total time required for the droplet to freeze. It is important to note that determining the total freezing time poses a significant challenge even when the same substrate-liquid combination is employed. This is because the freezing time is strongly influenced by transient variations in humidity, substrate thickness, and external forces such as vibration and gravitational acceleration. Therefore, accurate measurements of the frozen droplet height require consideration of the droplet's geometry.

The comparative analysis presented in Fig. 3.5 (a) encompasses four distinct metal substrates: Aluminum, Brass, Copper, and Titanium. Furthermore, the study considers water droplets with volumes of $3\mu l$, $6\mu l$, and $10\mu l$. It can be observed that the two-triangle approach can predict the frozen droplet height within $\pm 10\%$, regardless of the thermal properties of the substrate and the volume of the drop corresponding to the capillary length scale. The heat transfer model prediction constitutes the thermophysical properties of the system, primarily the thermal conductivity of the substrate, and from Fig. 3.5 the model predicts well for the substrate with the higher thermal conductivity within $\pm 10\%$. However, for substrates with lower thermal conductivity, the model fails to predict, as seen for the case of droplets 3 and $6\mu l$ on titanium substrates. This disagreement with the experimental results motivated us to further investigate the two-triangle approach.

Fig. 3.5 (b) illustrates the theoretical representation of the solid-liquid height ratio of a droplet relative to its density ratio ν , using the two-triangle and average contact angle approaches. From the figure it is evident that the average contact angle model tends to overestimate the drop height ratio compared to the two-triangle approach. This discrepancy can be confirmed from the case of water ($\nu = 0.917$). Both models predict that the height ratio decreases with an increase in the density ratio. It is crucial to note that for a density ratio of 1, the average contact angle approach diverges, indicating a limitation in its applicability. To overcome this limitation, a value of ν shown in the Fig. 3.5 (b) is slightly less than one. In contrast, the proposed two-triangle approach has the advantage of accurately predicting the height ratio for $\nu \geq 1$. The two-triangle approach provides reasonable agreement of the height ratio with the experimental data, especially at higher density ratios. This is confirmed for the case of paraffin wax ($\nu = 1.1$), where the height ratio estimated using the two-triangle approach is compared against experimental measurements from the work of Pritam et al.[88]. This highlights the predictive capability of the proposed two-triangle method in capturing droplet behavior across a wider range of density ratios.

The tip angle (2α) for different density ratios is plotted in Fig. 3.5 (b) using the relationship discussed earlier. An increasing trend in the value of 2α can be observed as long as ρ_s is less than ρ_l , until ν reaches 1. However, once ρ_s surpasses ρ_l , a downward trend becomes evident. The schematic diagrams inscribed in Fig. 3.5 (b) indicate the formation of a tip when $\nu < 1$ and a dimple when $\nu > 1$ [49, 88]. The 2α for water and paraffin are 131° and 168° , respectively, which are in reasonable agreement with the literature [53, 54, 88].

3.6 Conclusion

In summary, the true universality of the frozen drop is determined by considering the shape of the drop. Therefore, we show universal behavior in the solid-liquid drop height ratio where $h_s = 1.2h_\ell$ regardless of experimental conditions. This has been shown for experiments ranging from symmetric to asymmetric drop. Parabolic flight experiments were performed to simulate microgravity, martian gravity and hypergravity. In this study, a geometric two-triangle model has been developed that predicts the height ratio with reasonable agreement of $\pm 10\%$. This was compared with the existing heat transfer and average contact angle approach. The model was further extended for a range of density ratios. A relation between the tip cone angle and the density ratio has also been developed.

Chapter 4

Dynamics of Successive Water Droplet Freezing

4.1 Abstract

The dynamics of droplet freezing on a cold substrate is critical in applications ranging from additive manufacturing to ice accumulation. This study expands the understanding of such phenomena by examining the behavior of consecutive droplets dosing onto a cold substrate and their transition into column-like ice structures on a macroscale. Using a jet-based dosing mechanism, we meticulously controlled the deposition of deionized and degasified water droplets onto a smooth copper substrate maintained at subzero temperatures. The experimental design varied the volume and frequency of the droplets systematically under four different conditions. Real-time shadowography and thermal imaging were utilized to capture morphological and thermal changes during the freezing process. The propagation of the ice-water interface is investigated to understand the remelting process for column-like ice structures between the drop interfaces. The effect of heat accumulation on the morphology of the ice structure is investigated using a noninvasive technique. Finally, an optimized condition was suggested that is suitable for macroscale ice printing.

4.2 Introduction

3D printing techniques have revolutionized the manufacturing industry with a wide range of applications [89]. The fundamental principle behind these applications is the solidification of the deposited material, which integrates the complexities of hydrodynamic behavior with the thermal phase transition of a deposited material [56]. Layer-by-layer solidification is one of the techniques used to fabricate 3D printed objects [14]. Drop-on-demand (DOD) technology, a key technique in this domain, enables the precise delivery of liquid quantities at exact moments, ensuring minimal waste and high fidelity to the intended design layers [90]. Despite technological advances made, understanding the complex interplay between rapid freezing of these droplets and the subsequent solid structures into which they form remains a critical area of research. The technique of successive liquid drop deposition, in which a drop is added to a droplet that is partially or fully solidified, is still under explored. Therefore, a comprehensive understanding of the factors that affect the morphology of the 3D printed structure is needed.

The successive drop deposition, also known as a “pile-up” of liquid drops, was first proposed by Haferl et al. [56], in which they suggested a mathematical model based on continuity and momentum equations coupled with the energy transfer equation in the Lagrangian formulation and then solved it numerically. Later, an experimental investigation was carried out to understand the physical mechanism of the accumulation of microdroplets, which reveals that the total solidification time can be affected by the thermal contact resistance at the interfaces of each droplet [56]. The successive deposition of drops using a DOD method involves impacting the droplet on a non-flat surface of the presolidified droplet [56]. This results in the oscillatory behavior of subsequent droplets as a result of inertial forces dominating capillary forces. In the numerical study by Chen et al. [58], it was observed that the new drop gradually

oscillates and dampens under the effect of dissipation and solidification. Heat transfer occurs from the top droplet to the substrate through the presolidified drops, and the bonding between each drop depends on whether the new drop melts the interface between the presolidified drop.

Chao et al. [91] proposed a classification of different types of bonding that can occur during this pile-up of microdroplet processes, including no bonding, partial bonding, ideal bonding, and excessive bonding. They observed that this bonding is highly influenced by the interface temperature (the temperature at the interface of two successive droplets), i.e. whether the remelting of the solidified drop occurred or not. Li et al. [59] developed a computational model to better understand the bond between successive drop interfaces using a front tracking method. A "ravine-like structure" was observed near the drop interface for the cases of no bonding and partial bonding.

In recent years, the focus of successive drop deposition has shifted from molten metal to water or water-based colloidal solution due to its applications in cryogenic 3D printing [14, 57]. Cryogenic 3D printing uses the rapid freezing properties of water by dispensing tiny droplets from a nozzle onto a precooled substrate, where they promptly crystallize. However, limited studies have been performed on "ice printing". In the study by Zheng et al. [30], picoliter-sized water droplets were deposited on a subcooled surface, forming pillar-shaped structures. The morphology of the structure was controlled by varying the frequency with which the drops were deposited. A similar study was performed by Garg et al. [61] where complex ice structures were generated by maneuvering the stages.

Previous investigations into the 3D printing of ice structures have predominantly focused on the microscale, employing droplets with volumes in the picoliter range.

Such scales, while valuable for fundamental studies, offer limited practical applicability for broader engineering and scientific purposes. Addressing this gap, our study expands the scope to macroscale ice printing by utilizing droplet volumes in the microliter range. In order to understand the fundamental phenomena of successive drop deposition on the macroscale, we explored four distinct scenarios, varying both the volume of the droplets and the frequency of their deposition, to examine the resultant morphology of the column-like ice structures. We have used a jet-based dosing technique to generate precise volumes at desired time intervals. Although our approach differs from conventional methodologies that deposit each successive droplet onto a fully solidified predecessor, our approach involves deposition onto partially solidified droplets. Furthermore, we analyze the temperature profiles across these scenarios to elucidate the effect of heat accumulation.

4.3 Experimental setup

For our experimental procedure, we used a custom-built experimental apparatus housed within a commercial protective case (Pelican case model 0500) to ensure both the safety of the equipment and control the surrounding environment. To generate the jet, a mobile surface analyzer (MSA, KRÜSS) was used. This device has previously shown its effectiveness in producing the consistent and controlled droplet deposition necessary for our study [32, 45]. A commercial image processing software called “ADVANCE” developed by KRÜSS was used to dose the desired volume of droplets at a given frequency. This software can be used to control the precise volume and frequency at which each droplet is deposited.

The working fluid used throughout our experiments was deionized and degasified water, chosen for its purity and reproducibility of the results. We meticulously maintained the flow rate at $(15 \pm 2 \mu\text{ls}^{-1})$, a rate that ensures a continuous jet that would

neither break up prematurely nor cause splashing upon contact with the substrate. This precise control allowed us to focus on the effects of varying the volume and frequency of the droplets. The substrate itself was ($60\text{mm} \times 60\text{mm} \times 1\text{mm}$) mirror-finished copper (sourced from McMaster Carr). This substrate was placed on top of a thermal electrical assembly (TEA), which gave us the ability to regulate the surface temperature with precision. The substrate temperature was maintained at -15°C . A thermal paste (purchased from Arctic Silver, thermal conductivity $\approx 8.7\text{W}/(\text{mK})$) was used to attach the substrate to the TEA cold plate.

For visual analysis, we captured shadowgraphy images using the built-in CMOS camera of the MSA. This technique allowed us to obtain high-contrast images of the droplets, which are essential for examining the shapes and structures of the droplets formed upon contact with the substrate. Thermal imaging was carried out using a high-speed thermal camera (A6700, FLIR Systems) with a resolution of 640×512 , set through a 17mm calibrated lens. This equipment was crucial for non-invasive measurement of the temperature profiles of the droplets and the substrate during the dosing and freezing process. The temperature data collected provided insight into the interplay between the thermal properties of the deposited material in the form of droplets and the substrate and the influence of the substrate temperature on the freezing process. Data analysis was performed using FLIR Research Studio software, which allows us to process the thermal images and extract quantitative temperature measurements under the different experimental conditions. The combination of shadowgraphy and thermal imaging provided a dual perspective of the physical form and thermal properties of the underlying phenomena.

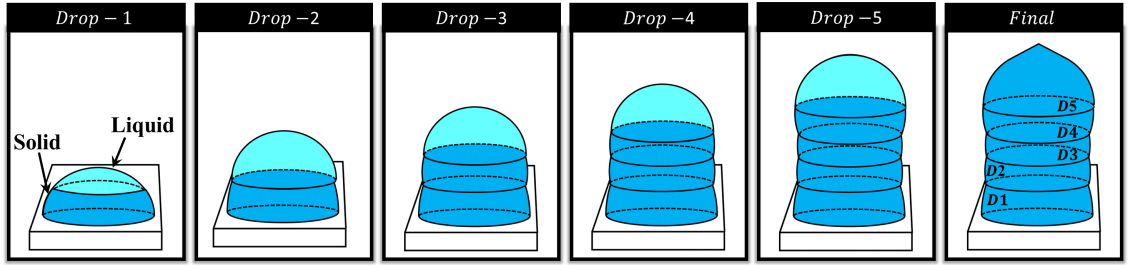


Figure 4.1: Schematic representation of the successive deposition of five droplets.

4.4 Results and Discussion

To investigate successive drop deposition of water on a macroscale, we deposited a series of five drops sequentially to generate an ice column-like structure, as shown in Fig. 4.1. This process begins with the deposition of the first droplet, that is, “*Drop - 1*”, on the precooled substrate followed by propagation of the freezing front, indicating a phase change. As we progress from “*Drop - 2*” to “*Drop - 5*,” additional drops are successively deposited on top of the previous ones. Each new droplet spreads over the partially solidified layer (solid-liquid interface) beneath it, thus increasing the height and volume of the column. The dotted lines in Fig.4.1 across the droplets suggest the interface between consecutive drops. The last panel of Fig. 4.1 reveals the completed structure of the column with five distinct droplets, labeled “*D1*” to “*D5*.” This process results in a pointed tip at the end, which is a result of the volume expansion of the water upon freezing.

Different morphological ice columns can be obtained by varying the volume of each droplet and the frequency at which each drop is deposited [56]. For the present study, we encountered four different shapes of the column by varying the dosing parameters. The representation of the experimental sequence for a droplet dosing is shown in Fig. 4.2, where the valve timing diagram is presented to illustrate the opening sequence in terms of 1 and 0 indicating that the nozzle is open or closed, respectively. The four lines, each corresponding to a different color, represent the four experimental

conditions investigated in this study. The black line ($V_c f_c$) represents the case where both the volume and the frequency of droplet dosing are kept constant. The regular and uniform pattern of ‘1’s and ‘0’s suggests a steady and uniform dosing rhythm. The green line ($V_v f_v$) is here; both volume and frequency are variable in this case. The red line ($V_c f_v$) represents the volume of the droplets that remains constant, but the frequency varies. Changes in the length of the ‘1’s indicate that the nozzle is opened for varying durations, corresponding to variable dosing intervals. Finally, the blue line ($V_v f_c$) resets the variable volume but the constant frequency. Differences in the width of ‘1’ s suggest changes in the amount of liquid dosed while maintaining a fixed frequency. This schematic is crucial for understanding how the dosing process was controlled and manipulated to create the different frozen columns observed in the study.

Table. 4.1 shows the quantitative values of volume and frequency considered for the four conditions investigated in this study. The first drop plays an essential role in determining the overall shape of the frozen ice column [60]. Therefore, the frequency at which the second drop is deposited is modified to ensure that the first drop is solidified to around 40 – 50%. The time taken by the freezing front to partially solidify the first droplet is theoretically predicted using the overall energy balance approach (OEB) along with the spherical cap assumption suggested in the previous chapter [43, 77]. This model successfully estimated the height of the first droplet. Using this droplet height as a boundary condition for the one-dimensional Stefan problem [51], we calculated the estimated time it took for the freezing front to solidify approximately 40% – 50% of the first droplet. This value serves as a reference point for designing the experimental framework for the current investigation. For variable frequency, the same criterion is applied to the second drop, whereas a basic linear function is used for the following droplets.

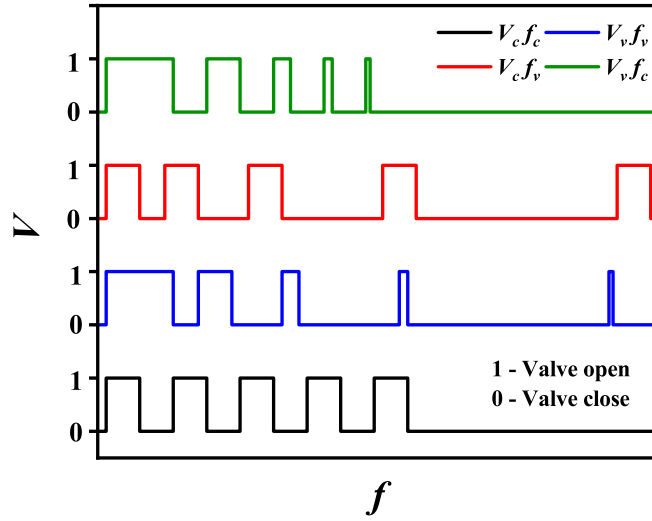


Figure 4.2: Schematic representation of the dosing sequence for each experimental condition, with ‘1’ indicating an open nozzle for liquid dosing and ‘0’ indicating no dosing.

		Drop-1	Drop-2	Drop-3	Drop-4	Drop-5
$V_c f_c$	Volume (μl)	2	2	2	2	2
	frequency (Hz)	0.5	0.5	0.5	0.5	
$V_v f_v$	Volume (μl)	4	2	1	0.5	0.25
	frequency (Hz)	0.66	0.36	0.16	0.09	
$V_c f_v$	Volume (μl)	2	2	2	2	2
	frequency (Hz)	0.66	0.36	0.16	0.09	
$V_v f_c$	Volume (μl)	4	2	1	0.5	0.25
	frequency (Hz)	0.5	0.5	0.5	0.5	

Table 4.1: Volume and frequency used for the current study are compiled for four cases. The study was presented in four different experimental settings, each varying the volume (V) and frequency (f) of the droplets in a controlled manner. The subscripts ‘ c ’ and ‘ v ’ denote constant and variable, respectively.

4.4.1 Ice column Morphology

Droplets exhibit different shapes and sizes depending on the specific conditions, suggesting that both volume and frequency have a significant impact on the shape of the column as they freeze. The final shape of the four cases from the experimental study is illustrated in Fig. 4.3. Fig. 4.3 (a) shows the shadowgraphic snapshots of the final shape of the column structure for the four conditions considered in this study. Fig. 4.3 (b) shows the corresponding thermal profiles of the droplets on a color-coded temperature scale. These profiles represent the temperature distribution within each droplet as it is deposited onto the substrate. It is evident from Fig. 4.3, that the final shape of each condition is significantly different. For $V_c f_c$, we observed a “bulb” or “flower bud”-like structure instead of the cylindrical structure that was observed for the other conditions. For example, $V_v f_v$, we observed that the first four drops are frozen symmetrically; however, the final drop is offset from the center axis of the column due to complete solidification and the formation of a pointy tip for the fourth drop before the final drop is deposited. In the case of $V_c f_v$ we dosed a constant volume of $2\mu l$, allowing the drop to partially freeze before dosing another drop. This showed a significant increase in the height of the pillar. Finally, for the case of $V_v f_c$, we observed a uniform cylindrical structure with the formation of a pointy tip at the end of the freezing.

The easiest way to analyze the bonding based on visual representation is to compare the curvature of the first drop with subsequent drops [59]. We can observe from Fig. 4.3 that for the cases where volume is constant ($V_c f_c$ and $V_c f_v$, we can observe that the circumference of the column increases, where for variable volume it decreases or remains uniform. This suggests that decent bonding can be achieved under a variable volume condition [59]. However, for a variable volume, the height of the column is restricted. This is because the volume of the final drop is $0.25\mu l$ and it

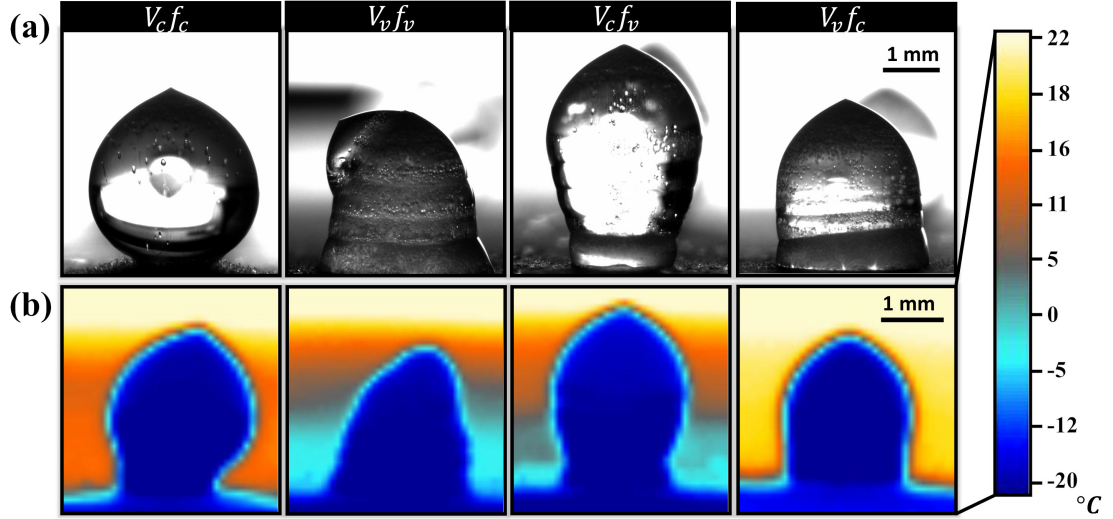


Figure 4.3: (a) Shadowgraphic and (b) thermal images of the final column-ice structure for four experimental conditions $V_c f_v$, $V_c f_c$, $V_v f_v$, and $V_v f_c$.

is practically not feasible to further decrease the volume size for successive droplets. Therefore, we can say that the structures generated by $V_c f_v$ are more practical than those generated by [91]. Therefore, further discussion centers on $V_c f_v$ by comparing it with other conditions.

4.4.2 Remelting and bonding

The bonding between successive drops is crucial to obtain stable and good-quality ice structures. This is achieved by remelting the solidified droplet when a new relatively high temperature drop is deposited on top of it [91]. Therefore, the propagation of the solid-liquid interface for the entire column formation process is investigated for all four conditions. Investigating the propagation of the freezing front can help us better understand the remelting process. Fig. 4.4 (a) shows the snapshots of the shadowgraphic images when each drop is deposited for $V_c f_v$. The solid-liquid interface is highlighted by a red-dashed line. The corresponding temporal evolution of the freezing front and the column height is shown in Fig. 4.4 (b).

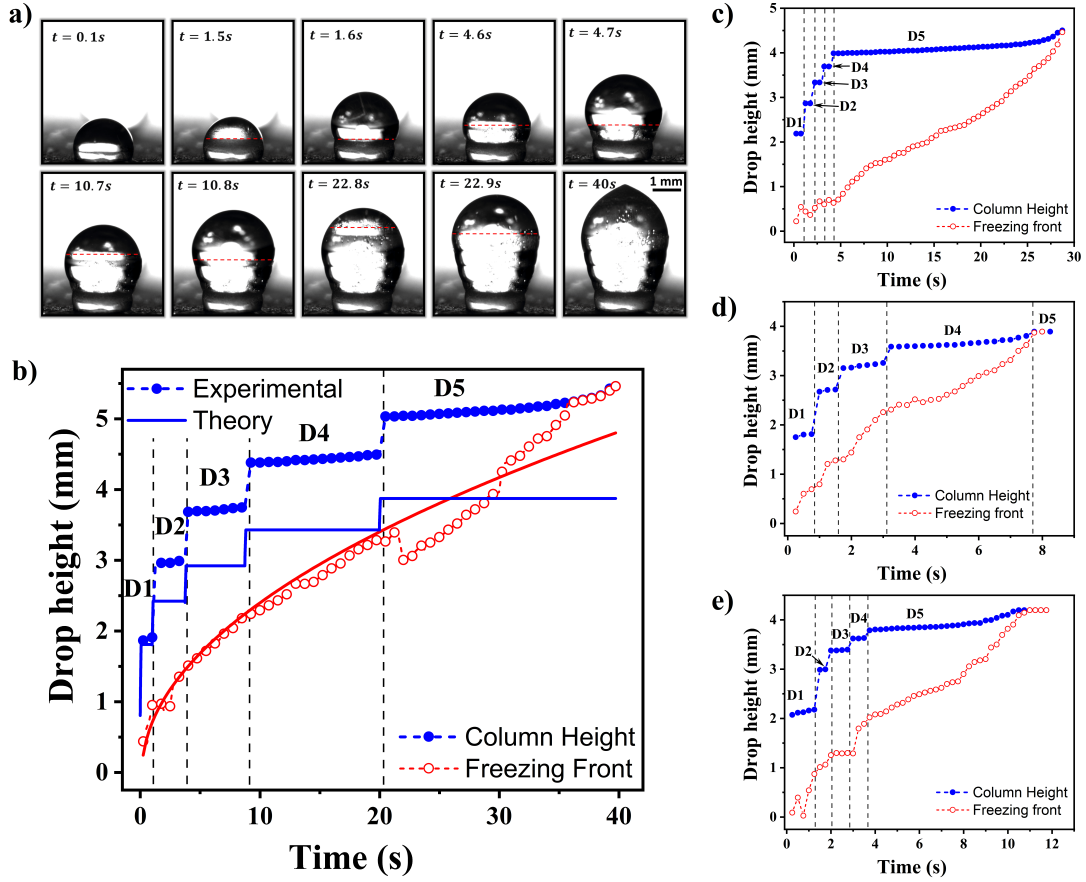


Figure 4.4: (a) Shadowgraphy images of each drop deposition and freezing front propagation (dotted red line) before the next drop along with corresponding time stamps. Graphs showing the progression of droplet height and the corresponding freezing front over time for the conditions (b) $V_c f_v$, (c) $V_c f_c$, (d) $V_v f_v$, and (e) $V_v f_c$.

From Fig. 4.4 (b), a closer investigation of the propagation of the freezing front, it can be observed that between D1-D2 and D4-D5, there is a noticeable decrease in the height of the freezing front. This decrease in the height of the freezing front suggests remelting of the solid-liquid interface, which is the primary requirement to ensure adequate bonding between the layers of the final product [59, 91]. However, we did not observe significant remelting between D2-D3 and D3-D4. The low time interval between two successive depositions is the main reason for the absence of remelting. This resulted in an increase in the circumference of the column as each drop is dosed.

To predict the height of the generated column, the OEB model proposed in Chapter 2 has been further analyzed with certain assumptions; such as, droplet is deposited on an ice-liquid interface, there was no effect of remelting, and the volume of the unfrozen frozen drop is not considered. Furthermore, the contact angle made by these drops is assumed to be constant and equal to the contact angle made by the first drop. Due to these critical assumptions, the predicted column height deviates from the experimental results from the second drop onward. However, the OEB model was able to predict the increasing trend in column height. This signifies the need for an improvement in the OEB model to predict the final column height for the successive drop-deposition condition. By ignoring the remelting effect, the one-dimensional Stefan equation $h_i = \sqrt{\frac{2k_i\Delta T}{\rho_i L}t}$ where the solid thermal conductivity (k), the solid density (ρ_s), the latent heat of the fusion (L_f), the difference in temperature ($\Delta T = T_m - T_c$) [51] can predict the propagation of the freezing front. However, the 1D Stefan equation under predicted the final height of the column.

However, for $V_c f_c$, as shown in Fig. 4.4 (c), since the droplets are deposited at a constant volume but faster frequency that did not allow the freezing front to propagate. The freezing front position remained almost constant until the dosing was stopped. Once dosing had stopped, a steady freezing front propagated, solidifying

the whole droplet. For variable volume conditions ($V_v f_v$ & $V_v f_c$), as shown in Fig. 4.4 (d and e), the volume of the drop decreases, resulting in the complete mixing of the unfrozen liquid and the new incoming drop. Because the volume of the new droplet is lower than that of the already solidifying drop, the remelting of the solid-liquid interface was very minimal. For $V_v f_v$ (shown in Fig. 4.4 (d)), $D5$ is deposited at very low frequency and, when deposited, the rest of the pillar is completely solidified. Because a smaller volume is deposited, no melting of the interface is observed, which shows no bonding condition.

4.4.3 Effect of heat accumulation

The heat transfer within the column-ice structure can be influenced by an increase in the column height, leading to the formation of a thicker ice layer. Consequently, this leads to a decrease in heat transfer efficiency as a result of the lower thermal conductivity of the ice [92]. When a new drop with a higher temperature is added, the heat begins to accumulate at the top of the column. The presence of the ice layer causes resistance, resulting in a gradual decrease in the temperature of the newly added drop. This process is referred to as heat accumulation[92]. For the current study of successive drop freezing, the accumulation of heat due to convection and radiation is negligible, compared to conduction [59]. As we increase the height of the ice structure by adding a droplet, heat accumulates in the upper region of the vertical column. This can be studied by observing the thermal behavior of consecutive droplets deposited on a cold substrate, with the intention of observing their freezing and the formation of a column-like structure. The temperature profiles shown in Fig. 4.5 demonstrate the temperature changes of each drop over time as it is dosed onto the substrate. Fig. 4.5 (a) illustrates the experimental thermal images for condition $V_c f_v$ with the corresponding time stamps. As additional mass is added through subsequent droplets, there is a notable increase in temperature.

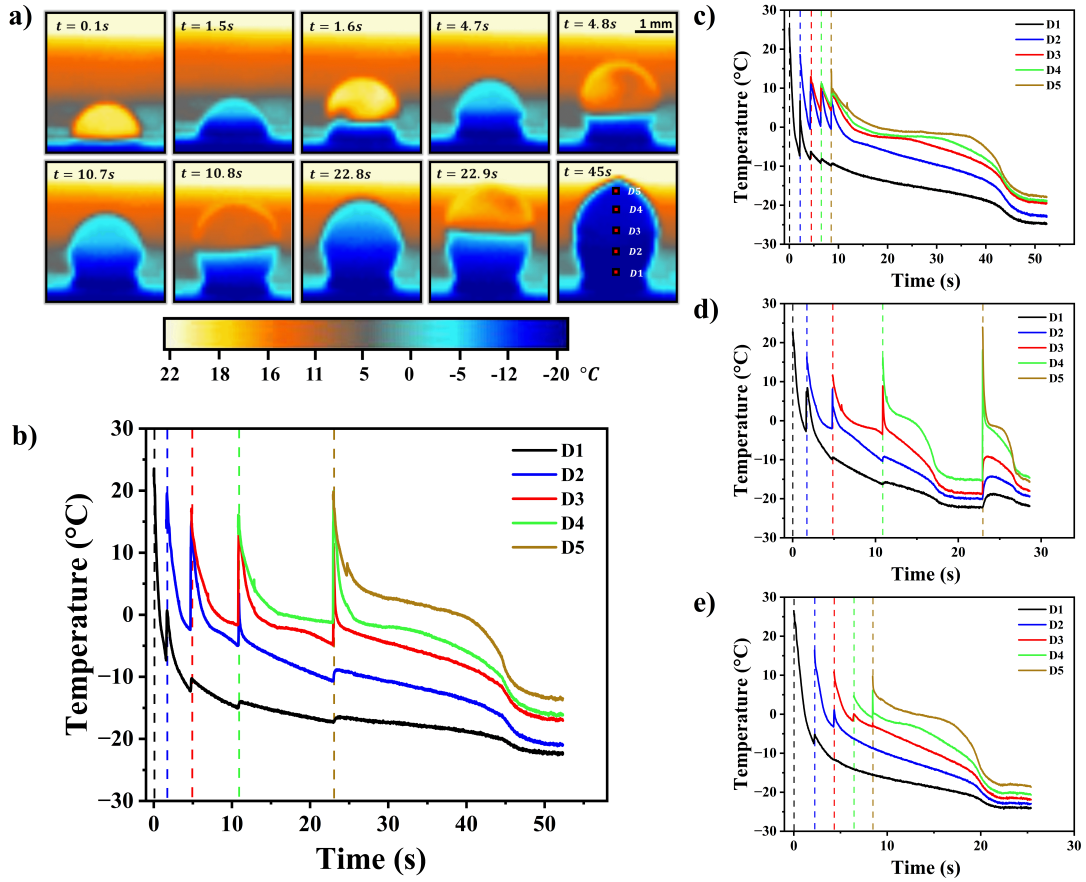


Figure 4.5: (a) Snapshots of thermal images of each drop deposition and solidification before the next drop along with corresponding time stamps. Locations at which the temperature profile are extracted are shown in final snapshot. Graphs illustrating the evolution of the thermal profile over time for the scenarios (b) $V_c f_v$, (c) $V_c f_c$, (d) $V_v f_v$, and (e) $V_v f_c$.

The evolution of the temperature of each droplet during the freezing process for all four conditions is shown in Fig. 4.5 (b-e). The vertical dotted lines indicate the time at which the successive drop is deposited. As mentioned above, heat accumulation occurs in the upper region of the vertical column. For example, in $V_c f_c$, due to faster mass addition at room temperature, the effect of heat accumulation is clearly observed, the temperature of the first drop at location D1 is below the melting temperature and has started to melt, while the other consecutive drop temperatures are approximately the melting temperature, indicating that no freezing has occurred. For $V_c f_v$, the temperature of the first three droplets decreases below the melting temperature, indicating gradual solidification. As the height of the column increases, due to the effect of thermal contact resistance, the D4 temperature closes the melting point. Although we observed freezing front propagation, due to heat accumulation, considerable melting was observed. This effect of heat accumulation can be reduced by decreasing the frequency with which the drop is deposited [92].

For variable volume and variable time, initially we observe a no-heat accumulation effect, since the amount of incoming mass at room temperature is reduced, but, as discussed earlier, the final drop is deposited on an already frozen column. This results in an increase in the overall temperature of the column at the end due to heat transfer through the solidified structure, as shown in Fig. 4.5 (d). However, for $V_v f_c$ no heat accumulation is observed. The sudden increase in temperature as a result of heat transfer is also very minimal compared to other conditions. However, the variable-volume condition with a decreasing volume is not practical for implementing 3D printing.

4.5 Conclusion

The experimental study presented herein provides a detailed examination of the freezing behavior of consecutive water droplets on a cold copper substrate under various dosing conditions. By systematically varying the volume and frequency of the droplets, we have observed and characterized the intricate relationship between the controlled dosing parameters and the resultant thermal and physical properties of the formed ice structures. Our findings indicate that both the volume and frequency of droplet deposition play a crucial role in dictating the growth rate and morphology of column-like ice structures. The bonding condition is analyzed by observing growth in the ice-water interface, taking into account the remelting from the addition of a new droplet. Furthermore, we analyzed the temperature profiles to understand the effect of heat accumulation in a macroscale ice structure. After carefully evaluating the results, we can say that $V_c f_v$ can be regarded the most optimized condition for the development of a 3D structure along the vertical direction.

Chapter 5

Conclusion and Future Work

5.1 Conclusion

This thesis presents a thorough examination of the dynamics and shape of freezing water droplets, which is essential for various industrial and scientific purposes. Each chapter of this thesis concludes with a summary of key findings and their significance. Thus, this section gives a summary of the collective impact of all the findings from a wider viewpoint.

In Chapter 2, our study investigated the simultaneous spreading and freezing of sessile droplets, particularly using a jet-based dosing technique. We did not observe the effect of supercooling for the jet-based technique because of the competition between heat transfer and mass addition. We employ a comprehensive theoretical model based on the Overall Energy Balance (OEB) approach to determine the transient spreading of TPCL considering heat transfer from the impinging cold substrate. Appropriate length, time, and temperature scales were used to non-dimensionalize the governing equations. Experimental findings were used to validate the theoretical prediction, and we observed a reasonable agreement of $\pm 5\%$. A decreasing trend in the spreading rate and an increase in the contact angle are observed as Ste increases. This signifies the influence of solidification on the damping of the movement of the TPCL. With a further increase in $Ste > 0.08$, we observed that TPCL is arrested as the mass is still

added. This is because the ice layer velocity is greater than the TPCL velocity. For $Ste > 0.08$, we observed that nucleation / recalescence occurred faster but the total freezing time is slower. This is due to an increase in the droplet height that causes the freezing front to travel longer. When the thermal conductivity of the substrate is decreased, the nucleation / recalescence time (t_{rec}) increases, resulting in a longer freezing time. Although the surface parameters influence the nucleation/ recalescence time, there is minimal difference in the freezing front rate.

In Chapter 3, the true universality of the frozen drop is determined by considering the shape of the drop. Therefore, we show universal behavior in the solid-liquid drop height ratio where $h_s = 1.2h_l$ regardless of the experimental conditions. This has been shown for experiments ranging from symmetric to asymmetric drop. Parabolic flight experiments were performed to simulate microgravity, Martian gravity, and hypergravity. In this study, a geometric two-triangle model has been developed that predicts the height ratio within reasonable agreement of $\pm 10\%$ (shown in Fig. 3.5). This was compared with the existing heat transfer and average contact angle approach. The model was further extended for a range of density ratios. A relation between the tip cone angle and the density ratio has also been developed.

In Chapter 4, we demonstrated that successive drop deposition is possible using a jet-based technique. Experimental parameters such as the volume of each drop and the frequency at which they are deposited play a key role in defining the final shape of the column/pillar. In the case where a constant volume of drop is maintained while the frequency of successive drop deposition is varied, we can achieve the maximum height. Compared to other cases where we observed distinct shapes such as a bulb/flower bud shape for $V_c f_c$. Therefore, a constant volume and variable time condition ($V_c f_v$) is recommended as an optimized condition to generate macroscale column-like ice structures.

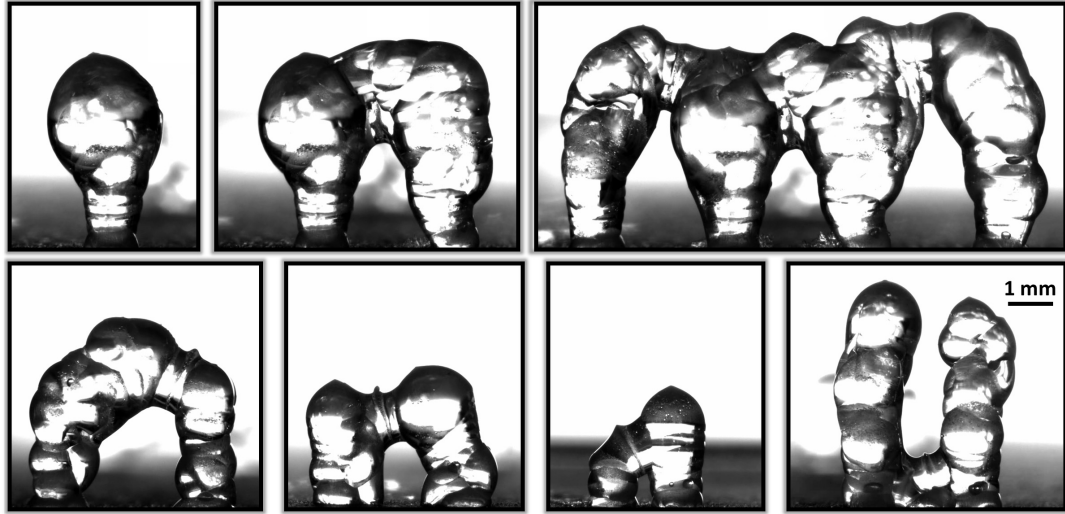


Figure 5.1: Ice structures printed using jet-based dosing technique

5.2 Future work

5.2.1 Ice-printing

The creation of column-shaped ice structures using a jet-based deposition technique has been a subject of our research, where we have successfully determined the optimal dosing conditions that produce the tallest structures with minimal thermal deviations. To refine this technique further, it is essential to establish a precise correlation between the volume of the droplets and the frequency of deposition, thereby enhancing the repeatability and precision of the process. Fig. 5.1 shows the complex ice structures generated using the jetting process. Nevertheless, the structures acquired were inconsistent due to constraints in the existing experimental setup. There is a pressing need for a method that reliably produces the desired shapes, allowing the construction of complex geometries, as demonstrated by Zheng et al. [30]. However, the intricacies of the structures presented by Zheng et al., involving picoliter volumes, do not yet translate to the larger scales required for practical 3D printing or freeze-casting applications. Moreover, the challenge of applying this method to

various colloidal solutions or ferrofluids in order to create similar column structures through freeze casting remains unexplored. Addressing this issue could bring significant advancements to the field [93].

Bibliography

- [1] F. Franks, *Water: a matrix of life*. Royal Society of Chemistry, 2000, vol. 21.
- [2] H. Wan, J. Bian, H. Zhang, and Y. Li, “Assessment of future climate change impacts on water-heat-salt migration in unsaturated frozen soil using coupmodel,” *Frontiers of Environmental Science & Engineering*, vol. 15, pp. 1–17, 2021.
- [3] H Zhang, “Theoretical analysis of spreading and solidification of molten droplet during thermal spray deposition,” *international journal of heat and mass transfer*, vol. 42, no. 14, pp. 2499–2508, 1999.
- [4] R. List, “Ice accretions on structures,” *Journal of Glaciology*, vol. 19, no. 81, pp. 451–465, 1977.
- [5] F. T. Lynch and A. Khodadoust, “Effects of ice accretions on aircraft aerodynamics,” *Progress in Aerospace Sciences*, vol. 37, no. 8, pp. 669–767, 2001.
- [6] M. Virk, M. Mustafa, and Q Hamdan, “Atmospheric ice accretion measurement techniques,” *The International Journal of Multiphysics*, vol. 5, no. 3, pp. 229–242, 2011.
- [7] S. Akhtar, M. Xu, M. Mohit, and A. P. Sasmito, “A comprehensive review of modeling water solidification for droplet freezing applications,” *Renewable and Sustainable Energy Reviews*, vol. 188, p. 113768, 2023.
- [8] A. Starostin, V. Strelnikov, L. A. Dombrovsky, S. Shoval, O. Gendelman, and E. Bormashenko, “Effect of asymmetric cooling of sessile droplets on orientation of the freezing tip,” *Journal of Colloid and Interface Science*, vol. 620, pp. 179–186, 2022.
- [9] I. V. Roisman and C. Tropea, “Wetting and icing of surfaces,” *Current opinion in colloid & interface science*, vol. 53, p. 101400, 2021.
- [10] X. Zhang, X. Wu, J. Min, and X. Liu, “Modelling of sessile water droplet shape evolution during freezing with consideration of supercooling effect,” *Applied Thermal Engineering*, vol. 125, pp. 644–651, 2017.
- [11] X. Zhang, X. Liu, J. Min, and X. Wu, “Shape variation and unique tip formation of a sessile water droplet during freezing,” *Applied Thermal Engineering*, vol. 147, pp. 927–934, 2019.
- [12] M. Sun, W. Kong, F. Wang, and H. Liu, “Impact freezing modes of supercooled droplets determined by both nucleation and icing evolution,” *International Journal of Heat and Mass Transfer*, vol. 142, p. 118431, 2019.

- [13] S. Schiaffino and A. A. Sonin, “Motion and arrest of a molten contact line on a cold surface: An experimental study,” *Physics of fluids*, vol. 9, no. 8, pp. 2217–2226, 1997.
- [14] Z. Li, M. Xu, J. Wang, and F. Zhang, “Recent advances in cryogenic 3d printing technologies,” *Advanced Engineering Materials*, vol. 24, no. 10, p. 2200245, 2022.
- [15] T. M. Schutzius *et al.*, “Physics of icing and rational design of surfaces with extraordinary icephobicity,” *Langmuir*, vol. 31, no. 17, pp. 4807–4821, 2015.
- [16] R. Grivet, A. Monier, A. Huerre, C. Josserand, and T. Séon, “Contact line catch up by growing ice crystals,” *Physical Review Letters*, vol. 128, no. 25, p. 254501, 2022.
- [17] D. Villanueva, D. Neubauer, B. Gasparini, L. Ickes, and I. Tegen, “Constraining the impact of dust-driven droplet freezing on climate using cloud-top-phase observations,” *Geophysical Research Letters*, vol. 48, no. 11, e2021GL092687, 2021.
- [18] A. Bogdan, *Ice clouds: Atmospheric ice nucleation concept versus the physical chemistry of freezing atmospheric drops*, 2018.
- [19] B. Kärcher and A. Seifert, “On homogeneous ice formation in liquid clouds,” *Quarterly Journal of the Royal Meteorological Society*, vol. 142, no. 696, pp. 1320–1334, 2016.
- [20] D. L. Mitchell and W. Finnegan, “Modification of cirrus clouds to reduce global warming,” *Environmental Research Letters*, vol. 4, no. 4, p. 045102, 2009.
- [21] C. James, G. Purnell, and S. J. James, “A review of novel and innovative food freezing technologies,” *Food and bioprocess technology*, vol. 8, pp. 1616–1634, 2015.
- [22] K. Overhoff, K. Johnston, J. Tam, J. Engstrom, and R. Williams III, “Use of thin film freezing to enable drug delivery: A review,” *Journal of Drug Delivery Science and Technology*, vol. 19, no. 2, pp. 89–98, 2009.
- [23] G. Tian, Z. Lu, K. Miao, Z. Ji, H. Zhang, and D. Li, “Formation mechanism of cracks during the freeze drying of gelcast ceramic parts,” *Journal of the American Ceramic Society*, vol. 98, no. 10, pp. 3338–3345, 2015.
- [24] I. B. Sebastião, B. Bhatnagar, and S. Tchessalov, “A kinetic model for spray-freezing of pharmaceuticals,” *Journal of Pharmaceutical Sciences*, vol. 110, no. 5, pp. 2047–2062, 2021.
- [25] Z. Wang, W. Finlay, M. Peppler, and L. Sweeney, “Powder formation by atmospheric spray-freeze-drying,” *Powder Technology*, vol. 170, no. 1, pp. 45–52, 2006.
- [26] B. Liu, H. Hu, L. Bi, and P. E. Theodorakis, “Analysis of the characteristics of the gas–liquid mixed artificial snow-making,” *International Journal of Refrigeration*, vol. 149, pp. 155–167, 2023.

- [27] Y. Bozkurt and E. Karayel, “3d printing technology; methods, biomedical applications, future opportunities and trends,” *Journal of Materials Research and Technology*, vol. 14, pp. 1430–1450, 2021.
- [28] Z. Tan, C. Parisi, L. Di Silvio, D. Dini, and A. E. Forte, “Cryogenic 3d printing of super soft hydrogels,” *Scientific reports*, vol. 7, no. 1, p. 16 293, 2017.
- [29] M.-A. Shahbazi, M. Ghalkhani, and H. Maleki, “Directional freeze-casting: A bioinspired method to assemble multifunctional aligned porous structures for advanced applications,” *Advanced Engineering Materials*, vol. 22, no. 7, p. 2 000 033, 2020.
- [30] F. Zheng, Z. Wang, J. Huang, and Z. Li, “Inkjet printing-based fabrication of microscale 3d ice structures,” *Microsystems & Nanoengineering*, vol. 6, no. 1, p. 89, 2020.
- [31] M. Jin, R. Sanedrin, D. Frese, C. Scheithauer, and T. Willers, “Replacing the solid needle by a liquid one when measuring static and advancing contact angles,” *Colloid and Polymer Science*, vol. 294, no. 4, pp. 657–665, 2016.
- [32] A. Ahmed, R. Sanedrin, T. Willers, and P. R. Waghmare, “The effect of dynamic wetting pressure on contact angle measurements,” *Journal of Colloid and Interface Science*, vol. 608, pp. 1086–1093, 2022.
- [33] S. Moghtadernejad, C. Lee, and M. Jadidi, “An introduction of droplet impact dynamics to engineering students,” *Fluids*, vol. 5, no. 3, p. 107, 2020.
- [34] J Madejski, “Solidification of droplets on a cold surface,” *International journal of heat and mass transfer*, vol. 19, no. 9, pp. 1009–1013, 1976.
- [35] Y. Yao, C. Li, Z. Tao, R. Yang, and H. Zhang, “Experimental and numerical study on the impact and freezing process of a water droplet on a cold surface,” *Applied Thermal Engineering*, vol. 137, pp. 83–92, 2018.
- [36] S. Chang, H. Song, and K. Wu, “Experimental investigation on impact dynamics and freezing performance of water droplet on horizontal cold surface,” *Sustainable Energy Technologies and Assessments*, vol. 45, p. 101 128, 2021.
- [37] W. Kong, L. Wang, P. Bian, and H. Liu, “Effect of surface wettability on impact-freezing of supercooled large water droplet,” *Experimental Thermal and Fluid Science*, vol. 130, p. 110 508, 2022.
- [38] X. Zhang, X. Liu, X. Wu, and J. Min, “Impacting-freezing dynamics of a supercooled water droplet on a cold surface: Rebound and adhesion,” *International Journal of Heat and Mass Transfer*, vol. 158, p. 119 997, 2020.
- [39] R. Zhang, P. Hao, X. Zhang, and F. He, “Supercooled water droplet impact on superhydrophobic surfaces with various roughness and temperature,” *International Journal of Heat and Mass Transfer*, vol. 122, pp. 395–402, 2018.
- [40] W.-Z. Fang, F. Zhu, W.-Q. Tao, and C. Yang, “How different freezing morphologies of impacting droplets form,” *Journal of Colloid and Interface Science*, vol. 584, pp. 403–410, 2021.

- [41] Y. Shang, X. Liu, B. Bai, and X. Zhong, “Central-pointy to central-concave icing transition of an impact droplet by increasing surface subcooling,” *International Communications in Heat and Mass Transfer*, vol. 108, p. 104326, 2019.
- [42] R. De Ruiter, P. Colinet, P. Brunet, J. H. Snoeijer, and H. Gelderblom, “Contact line arrest in solidifying spreading drops,” *Physical review fluids*, vol. 2, no. 4, p. 043602, 2017.
- [43] D. Erickson, B. Blackmore, and D. Li, “An energy balance approach to modeling the hydrodynamically driven spreading of a liquid drop,” *Colloids and Surfaces A: Physicochemical and Engineering Aspects*, vol. 182, no. 1-3, pp. 109–122, 2001.
- [44] S. Farzana, A. Baldygin, and P. R. Waghmare, “Experimental and theoretical investigation of the effects of pressure on the hydrodynamically driven droplet spreading,” *Chemical Engineering Science*, vol. 254, p. 117644, 2022.
- [45] A. Baldygin *et al.*, “Effect of gravity on the spreading of a droplet deposited by liquid needle deposition technique,” *npj Microgravity*, vol. 9, no. 1, p. 49, 2023.
- [46] J. E. Castillo, Y. Huang, Z. Pan, and J. A. Weibel, “Quantifying the pathways of latent heat dissipation during droplet freezing on cooled substrates,” *International Journal of Heat and Mass Transfer*, vol. 164, p. 120608, 2021.
- [47] S. Jung, M. K. Tiwari, N. V. Doan, and D. Poulikakos, “Mechanism of supercooled droplet freezing on surfaces,” *Nature communications*, vol. 3, no. 1, pp. 1–8, 2012.
- [48] M. Schremb, J. M. Campbell, H. K. Christenson, and C. Tropea, “Ice layer spreading along a solid substrate during solidification of supercooled water: Experiments and modeling,” *Langmuir*, vol. 33, no. 19, pp. 4870–4877, 2017.
- [49] J. H. Snoeijer and P. Brunet, “Pointy ice-drops: How water freezes into a singular shape,” *American Journal of Physics*, vol. 80, no. 9, pp. 764–771, 2012.
- [50] A. Schetnikov, V. Matiunin, and V. Chernov, “Conical shape of frozen water droplets,” *American Journal of Physics*, vol. 83, no. 1, pp. 36–38, 2015.
- [51] D. Anderson, M. G. Worster, and S. Davis, “The case for a dynamic contact angle in containerless solidification,” *Journal of crystal growth*, vol. 163, no. 3, pp. 329–338, 1996.
- [52] F. Boulogne and A. Salonen, “Drop freezing: Fine detection of contaminants by measuring the tip angle,” *Applied Physics Letters*, vol. 116, no. 10, p. 103701, 2020.
- [53] A. G. Marin, O. R. Enriquez, P. Brunet, P. Colinet, and J. H. Snoeijer, “Universality of tip singularity formation in freezing water drops,” *Physical review letters*, vol. 113, no. 5, p. 054301, 2014.
- [54] M. F. Ismail and P. R. Waghmare, “Universality in freezing of an asymmetric drop,” *Applied Physics Letters*, vol. 109, no. 23, 2016.

- [55] S Haferl and D Poulikakos, “Transport and solidification phenomena in molten microdroplet pileup,” *Journal of Applied Physics*, vol. 92, no. 3, pp. 1675–1689, 2002.
- [56] S Haferl and D Poulikakos, “Experimental investigation of the transient impact fluid dynamics and solidification of a molten microdroplet pile-up,” *International journal of heat and mass transfer*, vol. 46, no. 3, pp. 535–550, 2003.
- [57] C. W. Visser, R. Pohl, C. Sun, G.-W. Römer, and D. Lohse, “Toward 3d printing of pure metals by laser-induced forward transfer,” *Advanced materials*, no. 27, pp. 4087–4092, 2015.
- [58] C. Chen, J. Huang, H. Yi, and Y. Zhang, “Research on the solidified morphologies of successive pileup metal droplets,” *Journal of Mechanical Science and Technology*, vol. 34, pp. 3197–3205, 2020.
- [59] W. Li *et al.*, “Computational study on structures of vertical columns formed by successive droplets,” *Journal of Materials Processing Technology*, vol. 288, p. 116 903, 2021.
- [60] Z. Jin, X. Cheng, and Z. Yang, “Experimental investigation of the successive freezing processes of water droplets on an ice surface,” *International Journal of Heat and Mass Transfer*, vol. 107, pp. 906–915, 2017.
- [61] A. Garg, S. S. Yerneni, P. Campbell, P. R. LeDuc, and O. B. Ozdoganlar, “Freeform 3d ice printing (3d-ice) at the micro scale,” *Advanced Science*, vol. 9, no. 27, p. 2 201 566, 2022.
- [62] Ž. P. Kačarević *et al.*, “An introduction to 3d bioprinting: Possibilities, challenges and future aspects,” *Materials*, vol. 11, no. 11, p. 2199, 2018.
- [63] S. D. Aziz and S. Chandra, “Impact, recoil and splashing of molten metal droplets,” *International journal of heat and mass transfer*, vol. 43, no. 16, pp. 2841–2857, 2000.
- [64] D Sivakumar and H Nishiyama, “Spreading and solidification of a molten metal droplet impinging on a heated surface,” *International journal of heat and mass transfer*, vol. 47, no. 19-20, pp. 4469–4478, 2004.
- [65] V. Thiévenaz, T. Séon, and C. Josserand, “Solidification dynamics of an impacted drop,” *Journal of Fluid Mechanics*, vol. 874, pp. 756–773, 2019.
- [66] R. Dykhuizen, “Review of impact and solidification of molten thermal spray droplets,” *Journal of thermal spray technology*, vol. 3, pp. 351–361, 1994.
- [67] L. Huang, Z. Liu, Y. Liu, Y. Gou, and L. Wang, “Effect of contact angle on water droplet freezing process on a cold flat surface,” *Experimental thermal and fluid science*, vol. 40, pp. 74–80, 2012.
- [68] G. Chaudhary and R. Li, “Freezing of water droplets on solid surfaces: An experimental and numerical study,” *Experimental Thermal and Fluid Science*, vol. 57, pp. 86–93, 2014.

- [69] H.-M. Kwon, A. T. Paxson, K. K. Varanasi, and N. A. Patankar, “Rapid deceleration-driven wetting transition during pendant drop deposition on superhydrophobic surfaces,” *Physical review letters*, vol. 106, no. 3, p. 036 102, 2011.
- [70] L. Menglong, S. Mengjie, M. Zhenjun, W. Xiaotao, and Z. Long, “A modeling study of sessile water droplet on the cold plate surface during freezing under natural convection with gravity effect considered,” *International Journal of Multiphase Flow*, vol. 143, p. 103 749, 2021.
- [71] W. Kong and H. Liu, “A theory on the icing evolution of supercooled water near solid substrate,” *International Journal of Heat and Mass Transfer*, vol. 91, pp. 1217–1236, 2015.
- [72] W. Kong and H. Liu, “Unified icing theory based on phase transition of supercooled water on a substrate,” *International Journal of Heat and Mass Transfer*, vol. 123, pp. 896–910, 2018.
- [73] A. Starostin, V. Strelnikov, L. A. Dombrovsky, S. Shoval, and E. Bormashenko, “On the universality of shapes of the freezing water droplets,” *Colloid and Interface Science Communications*, vol. 47, p. 100 590, 2022.
- [74] X. Zhang, X. Liu, X. Wu, and J. Min, “Simulation and experiment on supercooled sessile water droplet freezing with special attention to supercooling and volume expansion effects,” *International Journal of Heat and Mass Transfer*, vol. 127, pp. 975–985, 2018.
- [75] H. Zhang, Y. Zhao, R. Lv, and C. Yang, “Freezing of sessile water droplet for various contact angles,” *International journal of thermal sciences*, vol. 101, pp. 59–67, 2016.
- [76] J.-P. Delplanque and R. Rangel, “An improved model for droplet solidification on a flat surface,” *Journal of materials science*, vol. 32, no. 6, pp. 1519–1530, 1997.
- [77] M Pasandideh-Fard, R Bhola, S Chandra, and J Mostaghimi, “Deposition of tin droplets on a steel plate: Simulations and experiments,” *International Journal of Heat and Mass Transfer*, vol. 41, no. 19, pp. 2929–2945, 1998.
- [78] P.-G. De Gennes, “Wetting: Statics and dynamics,” *Reviews of modern physics*, vol. 57, no. 3, p. 827, 1985.
- [79] M Pasandideh-Fard, Y. Qiao, S. Chandra, and J. Mostaghimi, “Capillary effects during droplet impact on a solid surface,” *Physics of fluids*, vol. 8, no. 3, pp. 650–659, 1996.
- [80] J. D. Bernardin, I. Mudawar, C. B. Walsh, and E. I. Franses, “Contact angle temperature dependence for water droplets on practical aluminum surfaces,” *International journal of heat and mass transfer*, vol. 40, no. 5, pp. 1017–1033, 1997.

- [81] J.-W. Song and L.-W. Fan, “Temperature dependence of the contact angle of water: A review of research progress, theoretical understanding, and implications for boiling heat transfer,” *Advances in colloid and interface science*, vol. 288, p. 102 339, 2021.
- [82] A Raveh, Z. Tsameret, and E Grossman, “Surface characterization of thin layers of aluminium oxide,” *Surface and Coatings Technology*, vol. 88, no. 1-3, pp. 103–111, 1997.
- [83] M Stiti, G. Castanet, A Labergue, and F Lemoine, “Icing of a droplet deposited onto a subcooled surface,” *International Journal of Heat and Mass Transfer*, vol. 159, p. 120 116, 2020.
- [84] M. Santos, S Velasco, and J. White, “Simulation analysis of contact angles and retention forces of liquid drops on inclined surfaces,” *Langmuir*, vol. 28, no. 32, pp. 11 819–11 826, 2012.
- [85] A. ElSherbini and A. Jacobi, “Liquid drops on vertical and inclined surfaces: Ii. a method for approximating drop shapes,” *Journal of colloid and interface science*, vol. 273, no. 2, pp. 566–575, 2004.
- [86] A. Ahmed, B. A. Fleck, and P. R. Waghmare, “Maximum spreading of a ferrofluid droplet under the effect of magnetic field,” *Physics of Fluids*, vol. 30, no. 7, 2018.
- [87] M. E. Bonomo, “Analyzing the singularities of freezing sessile water droplets,” 2013.
- [88] P. K. Roy, S. Shoval, N. Shvalb, L. A. Dombrovsky, O. V. Gendelman, and E. Bormashenko, “Apple-like shape of freezing paraffin wax droplets and its origin,” 2023.
- [89] L. Murr, “A metallographic review of 3d printing/additive manufacturing of metal and alloy products and components,” *Metallography, Microstructure, and Analysis*, vol. 7, pp. 103–132, 2018.
- [90] Z. Jiao, F. Li, L. Xie, X. Liu, B. Chi, and W. Yang, “Experimental research of drop-on-demand droplet jetting 3d printing with molten polymer,” *Journal of Applied Polymer Science*, vol. 135, no. 9, p. 45 933, 2018.
- [91] Y.-p. Chao, L.-h. Qi, H.-s. Zuo, J. Luo, X.-h. Hou, and H.-j. Li, “Remelting and bonding of deposited aluminum alloy droplets under different droplet and substrate temperatures in metal droplet deposition manufacture,” *International Journal of Machine Tools and Manufacture*, vol. 69, pp. 38–47, 2013.
- [92] M. Liu, H. Yi, H. Cao, R. Huang, and L. Jia, “Heat accumulation effect in metal droplet-based 3d printing: Evolution mechanism and elimination strategy,” *Additive Manufacturing*, vol. 48, p. 102 413, 2021.
- [93] S. Deville, “Freeze-casting of porous ceramics: A review of current achievements and issues,” *Advanced Engineering Materials*, vol. 10, no. 3, pp. 155–169, 2008.

Appendix A:

A parametric study was conducted to determine the limitations of the overall energy balance model of the simultaneous droplet spreading and freezing process. From this study, phase plots were produced as shown in Fig. A.1. This contour plot shows the variation of ξ (the initial maximum drop spreading in comparison with the diameter of the jet) with respect to various Reynolds, Weber and Stefan numbers. Fig. A.1(a) illustrates the relationship between the spreading ratio and the parameters Ste and Re . Our research indicates that for low values of Re , the spreading ratio remains consistently low, regardless of the change in Ste . This phenomenon can be attributed to the rapid arrest of TPCLs at higher Ste values. In contrast, as Re increases, the spreading ratio also shows an increasing trend, indicating the growing influence of the inertial forces on spreading. Fig. A.1 (b) illustrates the change in spreading ratio as a function of We and Ste . Here, the dotted curved line depicts the approximate inflection points. It denotes the boundary between the We and Ste dominant flow regimes. We observe that for a constant Ste , the spreading increases as the We increases in the We dominant regime and remains nearly unchanged in the Ste dominant regime. This analysis can help us better understanding the scalability of the current study for various applications.

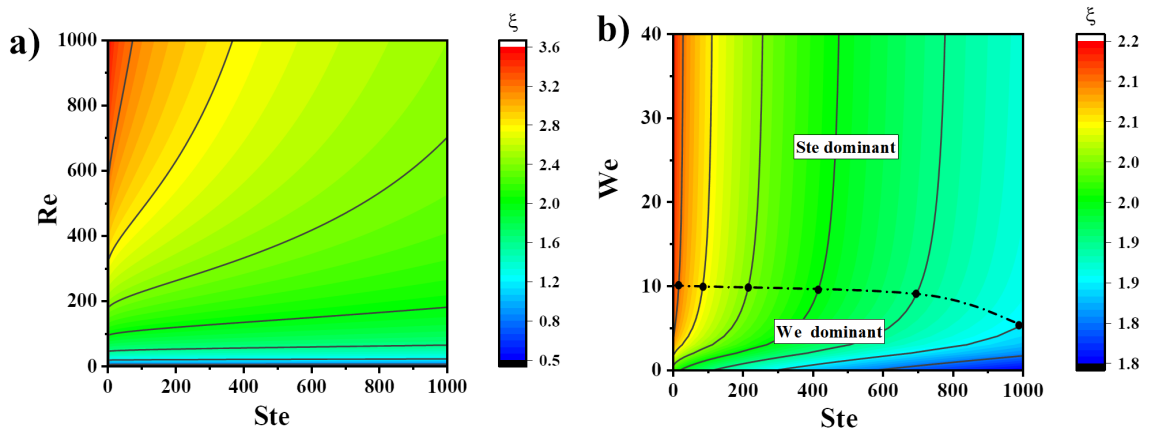


Figure A.1: Phaseplots showing the variation in the spreading ratio ξ with respect to a) Reynolds (Re) and Stefan (Ste) numbers, b) Weber (We) and Stefan (Ste) numbers. The colour bar represents the different values of spreading ratio ξ